Physical characterization of the deep-space debris WT1190F: a testbed for advanced SSA techniques[☆]

Alberto Buzzoni[*]

INAF - Osservatorio di Astrofisica e Scienza dello Spazio, Via Gobetti 93/3 40129 Bologna Italy

Giuseppe Altavilla

INAF - Osservatorio Astronomico di Roma, Via Frascati 33 00040 Monte Porzio Catone (RM), Italy

Siwei Fan, Carolin Frueh

School of Aeronautics and Astronautics, Purdue University, 701 W. Stadium Ave. West Lafayette, IN 47907-2045 USA

Italo Foppiani

INAF - Osservatorio di Astrofisica e Scienza dello Spazio, Via Gobetti 93/3 40129 Bologna Italy

Marco Micheli

ESA SSA-NEO Coordination Centre, ESRIN, Frascati, Italy
INAF - Osservatorio Astronomico di Roma, Via Frascati 33 00040 Monte Porzio Catone (RM), Italy

Jaime Nomen, Noelia Sánchez-Ortiz

DEIMOS Space S.L.U., Ronda de Poniente 19, 2-2, Tres Cantos, Madrid 28760, Spain

Abstract

We report on extensive BVR_cI_c photometry and low-resolution ($\lambda/\Delta\lambda \sim 250$) spectroscopy of the deep-space debris WT1190F, which impacted Earth offshore from Sri Lanka, on 2015 November 13. In spite of its likely artificial origin (as a relic of some past lunar mission), the case offered important points of discussion for its suggestive connection with the envisaged scenario for a (potentially far more dangerous) natural impactor, like an asteroid or a comet.

Our observations indicate for WT1190F an absolute magnitude $R_c = 32.45_{\pm 0.31}$, with a flat dependence of reflectance on the phase angle, such as $dR_c/d\phi \sim 0.007_{\pm 2}$ mag deg^{-1}. The detected short-timescale variability suggests that the body was likely spinning with a period twice the nominal figure of $P_{\rm flash} = 1.4547_{\pm 0.0005}$ s, as from the observed lightcurve. In the BVR_cI_c color domain, WT1190F closely resembled the Planck deep-space probe. This match, together with a depressed reflectance around 4000 and 8500 Å may be suggestive of a "grey" (aluminized) surface texture.

The spinning pattern remained in place also along the object fiery entry in the atmosphere, a feature that may have partly shielded the body along its fireball phase perhaps leading a large fraction of its mass to survive intact, now lying underwater along a tight ($\sim 1 \times 80$ km) strip of sea, at a depth of 1500 meters or less.

Under the assumption of Lambertian scatter, an inferred size of $216_{\pm 30}/\sqrt{\alpha/0.1}$ cm is obtained for WT1190F. By accounting for non-gravitational dynamical perturbations, the Area-to-Mass ratio of the body was in the range $(0.006 \leq AMR \leq 0.011)$ m^2 kg^{-1}.

Both these figures resulted compatible with the two prevailing candidates to WT1190F's identity, namely the Athena II Trans-Lunar Injection Stage of the Lunar Prospector mission, and the ascent stage of the Apollo 10 lunar module, callsign "Snoopy". Both candidates have been analyzed in some detail here through accurate 3D CAD design mockup modelling and BRDF reflectance rendering to derive the inherent photometric properties to be compared with the observations.

Keywords: Space debris – Deep-space Impactors – Space Situational Awareness techniques – Astrometry – Reflectance characterization

[☆]Based on observations collected at the Cassini Telescope of the Loiano Observatory, Italy, and the DeSS telescopes of the Mt. Niefla DEIMOS Observatory, Spain

[*]Corresponding author

1. Introduction

The puzzling case of WT1190F, a deep-space body, which entered Earth atmosphere off the Sri Lanka coast, last 2015 November 13, has been imposing attention worldwide to the media and to the scientific community involved in the Space Situational Awareness (SSA) activity as an outstanding opportunity to probe our reaction capabilities in order to effectively assess origin and physical nature of such extemporary visitors and appraise their potential threat for Earth.

With the only relevant exception of the few man-made sample return probes of interplanetary missions, like Genesis (Jenniskens et al., 2004), Stardust (Desai & Qualls, 2010; Jenniskens, 2010a), Hayabusa (Jenniskens et al., 2010b; Borovička et al., 2011; Fujita et al., 2011; Loelhe & Jenniskens, 2014), a common drawback when dealing with deep-space impactors (intending all those natural and artificial objects heading Earth at roughly the escape velocity, namely $v_{\rm esc} \sim 11$ km s^{-1}), is that they are usually discovered hours or just minutes before reaching our planet. The small asteroids 2008 TC_3 (Borovička & Charvát, 2009; Jenniskens et al., 2009), 2014 AA (Farnocchia et al., 2016) or even the disrupting Chelyabinsk event (Borovička et al., 2013; Popova et al., 2013) are remakable examples in this sense.

On the contrary, WT1190F offered a somewhat unique opportunity of deeper investigation as its fatal orbital evolution was successfully assessed (Gray, 2015) weeks in advance of its final fate over the sky of Sri Lanka (Jenniskens et al., 2016). This left room, therefore, for a wider and much deeper study of the inherent properties of this quite unusual and still mysterious body.

Following its nominal discovery by the Catalina Sky Survey, on 2015 October 3 (Matheny et al., 2015), WT1190F was first recognized as a possible small NEO asteroid captured in a HEO geocentric orbit. To a closer analysis, two further archive objects, namely UW8551D and UDA34A3, respectively from 2009 and 2013 observations, appeared to match the 2015 detection leading to suggest that we were actually dealing with the same object (Jenniskens et al., 2016). This extended dynamical information also set the stage for linking WT1190F to further 2009 and 2010 observations of the *bona fide* 9U01FF6 NEO (Birtwhistle, 2015), while supplementary back-identifications in 2011 and 2012 Pan-STARRS frames were eventually recovered by M. Micheli and E. Christensen (Farnocchia et al., 2016).

Altogether, these data show that WT1190F was in prograde chaotic motion around the Moon-Earth system, on orbital timescales between 19 and 40 days, along a very eccentric ($0.33 \leq e \leq 0.98$) translunar ($490\,000 \leq a \leq 655\,000$ km) trajectory with strongly variable inclination ($3^o \leq i \leq 78^o$). According to the latest observations, a forward-integrated orbit led eventually to predict for WT1190F an Earth impact on 2015 November 13, at 06:18 UTC, entering atmosphere with a steep incident angle $\sim 20^o$ at a speed of 10.6 km s^{-1} (Farnocchia, 2015).

Such a weak gravitational boundary with Earth made any attempt evidently pointless to firmly establish the nature of WT1190F from its dynamical signature alone. The only relevant hint, in this sense, relied on the high area-to-mass ratio (AMR) of the body, as inferred from the perturbing effect of solar radiation pressure (Gray, 2015). Coupled with the faint apparent magnitude, this feature better points to an anthropic origin of the object, possibly a metric-sized device related to some lunar mission, although of fully unknown origin.

As a part of the WT1190F worldwide observing campaign (see e.g. Jenniskens et al., 2016; Micheli et al., 2018, for a brief review in this regard), we have been tracking this so puzzling object from Spain and Italy along its last orbit up to very late moments before Earth impact with the aim to physically characterize the body and shed light on its real nature. In addition to the already published astrometric information (Buzzoni et al., 2015; Altavilla et al., 2015; Sánchez-Ortiz et al., 2015), we especially report here on unique photometric and spectroscopic observations, which allow us to assess in some detail the WT1190F geometric properties and Spectral Energy Distribution (SED). When coupled with accurate mock-up modelling and reflectance rendering, our results may add a valuable piece of information to constrain the possible candidate(s) and disclose the ultimate nature of WT1190F.

Our discussion will first overview, in Sec. 2, the observing database, presenting our full original observations from Loiano and Mt. Niefla. In Sec. 3 we will assess the issue of the absolute magnitude of WT1190F, a parameter of great importance to consistently relate any photometric piece of information with the inherently physical characteristic (size, geometry, composition, albedo etc.) of the target. We will also study here the effect of the illumination phase angle on target brightness, in most cases an explicit signature of the natural or artificial origin of the body.

Section 4 is fully devoted to the WT1190F atmosphere entry event of 2015 November 13. Along these special moments, and taking advantage of a closer distance to us, the target unveiled its finer spectro-photometric details, allowing us to set firm constraints on the (first hidden) spinning properties and lead to relevant conclusions about the possible location of the survived debris, in the Indian Ocean. A further relevant contribution of this section deals with the case of WT1190F as a unique template to assess the real capabilities of ground observatories to effectively tackle such potentially hazardous events in the future.

Colors, bolometric corrections and reflectance properties are presented and discussed in Sec. 5, leading to a hint of the possible structure and composition of the body. These results provide the reference framework to a more elaborated attempt, in Sec. 6, aimed at determining the possible identity of WT1190F, most probably as a relic

Email address: alberto.buzzoni@oabo.inaf.it (Alberto Buzzoni)

of some past lunar mission. Two outstanding cases are discussed, in this regard, dealing, from one hand, with a relatively near temporal horizon that focuses on the Lunar Prospector mission of year 1998. An alternative and more historical perspective will be tackled, however, where WT1190F might have been a silent witness of the early manned missions to the Moon of the late 60's, being the only survived Lunar Module LEM of the Apollo 10 mission. Our conclusions are finally summarized and further argumented in Sec. 7.

2. Observations

Bulk photometry of WT1190F can be found in the MPEC Distant Artificial Satellite Observation (DASO) Circulars,[1] which collect a total of 2079 entries for this object. However, DASO data focusses on astrometry, the apparent magnitudes being attached to the observations just as a rough on-frame estimate based on the reference astrometric grid of stars. This makes the overall photometric error to be strongly affected by systematics, essentially because the matching catalog magnitudes could be in a different band than observations, and astrometric reference stars may not necessarily be also photometric standards. A plus of this approach, however, is that it overcomes in principle any drawback due to non-photometric (cloudy) night conditions.

With these reservations in mind, the DASO dataset provides us with a historical timeline of WT1190F luminosity back to year 2009, as summarized in Fig. 1. In the plot we restrained to the data before 2015 November 12.6 UTC (thus excluding the last twelve hours before the final Earth approach). Out of the full set of data in this time range, some 125 magnitude estimates were carried out in the Johnson V band, while a total of 230 measurements have been collected in the generic (*bona fide* Johnson-Cousins) R band. One has to further add 34 observations to this set taken in unidentified bands, and especially an impressive sequence of 1271 Gunn r magnitudes by the 3.5 m Space Surveillance Telescope (SST) of Atom Site (USA, with IAU site code G45) aimed at probing target's short-timescale variability when it was midway to the Moon distance, on its route toward the last apogee transit, the night of 2015 October 25 UT, and in the final part of the returning orbit, on 2015 November 12 UT.

Due to the quite particular astronomical circumstances, that led target to enter Earth atmosphere in Sri Lanka during daytime, WT1190F's final approach of 2015 November 12-13 UTC was eventually tracked only by a few European telescopes suitably located near Earth's terminator. Of these, the Loiano (Italy, code 598) and Mt. Niefla (Spain, code Z66) observatories secured the most extended and accurate coverage of the event, complemented by key

[1]DASO Circulars are available in electronic form at the URL: *http://www.minorplanetcenter.net/iau/DASO/DASO.html*.

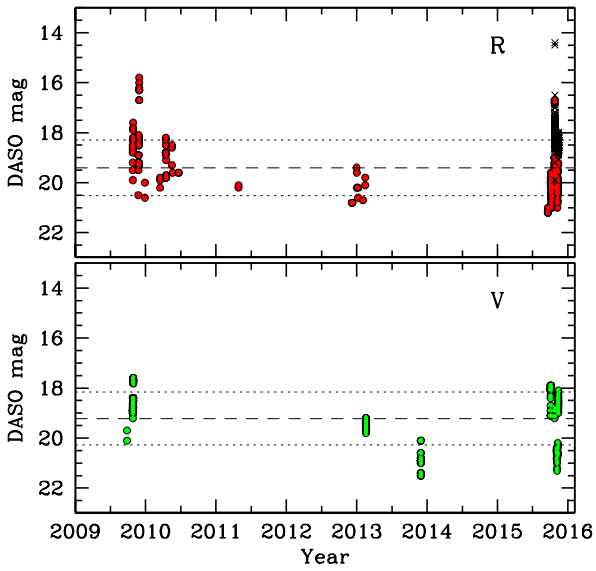

Figure 1: A historical timeline of the WT1190F V and R apparent magnitude, as from the DASO database, back to year 2009. The data collect observations for the "alias" objects UW8551D, UDA34A3 and 9U01FF6, later found to be identified with the same body. The full sample consists of 125 V and 230 R magnitude estimates. To these data one has to add a further set of 1271 Gunn r magnitudes by the G45 SST Atom Site Obs in late 2015 (oveplotted in the R panel as small "x" markers).

observations from the amateur telescopes of Great Shefford (UK, code J95), and Campo dei Fiori and Lumezzane (Italy, codes 204 and 130, respectively). According to the DASO database, a total of 419 astrometric measurements were collected along the falling trajectory, of which 348 provided a V magnitude, 58 an R magnitude and 13 were in unidentified or non-standard photometric bands.

2.1. The Loiano dataset

From Loiano, we probed WT1190F along the nights of November 7-8, and November 9-10, just after the last apogee passage, when the object was still well beyond the Moon distance, respectively some 515 000 and 420 000 km away from us. A third observing run was carried out the night of November 12-13 UTC, tracking the target up to one hour before its atmosphere entry in the dawn of November 13.

Observations have been carried out with the Cassini 1.52 m telescope. The on-board BFOSC camera covered a field of view of 13.2 × 13.0 arcmin, imaged with a 1370 × 1340 back-illuminated EEV CCD with 15μm pixel size. This led to a 0.58 arcsec px^{-1} plate scale across the field. Along the nights of November 7-8 and November 9-10 multicolor photometry was carried out in the Johnson-Cousins BVR_c bands, complemented by I_c magnitudes the night of November 12-13.

At translunar distances, the target appeared extremely faint (about $R_c \sim 20$) and its successful detection only relied on telescope non-sideral tracking capability, which

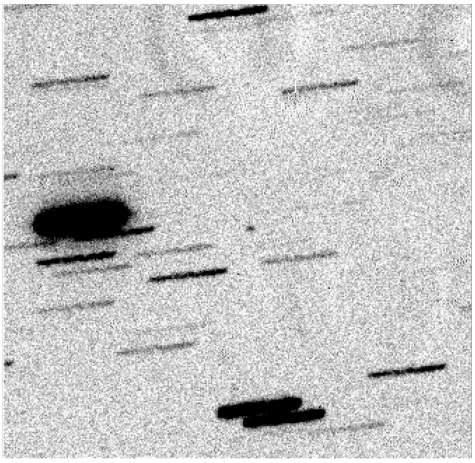

Figure 2: An illustrative frame of WT1190F detection at 01:21:34 UTC (mid-exposure time, see Table 1) of 2015 November 8. The target is imaged in the Johnson-Cousins R_c band with a 420 s exposure time. The cropped field here is 3.1 arcmin across. At the moment of this exposure, the object was 518 000 km away from us. Thanks to the "on-target" telescope tracking, WT1190F is clearly detected as a point source at the center of the image, with a magnitude $R_c = 20.54$.

allowed "on-target" photon stacking to greatly enhance the object S/N ratio on the CCD (Buzzoni et al., 2016, see Fig. 2 for an illustrative example). Although always observing under fair sky conditions, to a more accurate check, the night of Nov 9-10 eventually happened not to be entirely photometrical due to (hidden) patchy clouds in its second part. We have been able to fully recover photometry by differential correction, just relying on the large grid of stars in common with the target frame sequence, in order to confidently tie the "cloudy" photometry with the PG0231+051 Landolt (1992) standard stars observed at the beginning of the night and taken under photometric conditions. The same standard field was used for the night of November 12-13, while November 7-8 observations relied on the Rubin 149 calibrating field.

A consistent photometric calibration was achieved in the different bands, with a conservative uncertainty of ±0.10 mag for B and I_c bands, and ±0.05 mag for V and R_c, respectively. These figures have to be added in quadrature to the internal accuracy of target magnitudes, according to the observed S/N ratio, so that a fair estimate of our WT1190F magnitude uncertainty turns eventually to be 0.2 mag for the V and R_c bands and 0.3 mag for B and I_c. WT1190F was successfully detected in 15 frames (mostly in the R_c band) each night of November 7-8 and November 9-10. Given the quite "red" color of the target, its successful detection also in the V and B frames required a substantial increase of exposure time (up to 1200 s in B) compared to a reference figure of 420 s in R_c. A plot of our observations is reported in Fig. 3, while Table 1 reports a summary of the data, together with the inferred absolute magnitude,[2] according to the topocentric range estimate

[2]By definition, if the target range (d) is known in kilometers, then the "distance modulus" to 1 au reference distance can be computed as $(M - m) = -5\log(d) + 40.875$.

Table 1: The Loiano observations of 2015 November 7-8 and November 9-10

UTC[a] hh:mm:ss	Exp time [s]	Apparent mag	Band	log d[b] [km]	Absolute mag[d]	Phase[c] [deg]
2015 November 8 UTC						
00:48:58	300	20.47	R	5.7131	32.78	47.0
00:57:53	300	20.69	R	5.7128	33.00	47.0
01:13:23	420	20.44	R	5.7124	32.75	47.0
01:21:34	420	20.54	R	5.7122	32.85	47.0
01:29:19	420	20.09	R	5.7120	32.41	47.0
01:37:15	420	20.14	R	5.7118	32.46	47.0
02:01:38	600	20.85	V	5.7112	33.17	46.9
02:45:13	420	20.56	R	5.7102	32.88	46.8
02:59:49	1200	22.09	B	5.7099	34.42	46.8
03:16:09	600	20.91	V	5.7096	33.24	46.8
03:28:30	420	20.68	R	5.7093	33.01	46.8
03:38:07	420	20.34	R	5.7092	32.67	46.7
04:01:20	1200	21.80	B	5.7088	34.13	46.7
04:18:15	600	21.06	V	5.7085	33.39	46.7
04:35:55	420	20.25	R	5.7083	32.58	46.6
2015 November 10 UTC						
01:07:56*	420	20.24	R	5.6141	33.04	48.1
01:15:54*	420	20.13	R	5.6137	32.94	48.1
01:23:51	420	19.85	R	5.6133	32.66	48.0
01:31:43	420	19.88	R	5.6129	32.69	48.0
01:42:27*	420	19.87	R	5.6123	32.68	48.0
02:01:24*	420	19.93	R	5.6113	32.75	48.0
02:13:30	420	19.70	R	5.6107	32.52	47.9
02:52:06*	420	19.99	R	5.6089	32.82	47.9
03:02:01	600	20.44	V	5.6085	33.27	47.8
03:37:32	420	19.57	R	5.6069	32.41	47.8
03:48:51*	420	19.81	R	5.6064	32.65	47.8
04:03:56	1200	21.51	B	5.6058	34.36	47.7
04:21:05	420	19.45	R	5.6051	32.30	47.7
04:37:26	420	19.61	R	5.6045	32.46	47.7
04:57:34	420	19.44	R	5.6037	32.30	47.7

[a] At mid exposure. Entries with asterisks have their astrometry published in the DASO Circ. (Buzzoni et al., 2015).
[b] Target range according to Farnocchia's (2015) final orbit reconstruction.
[c] Topocentric ephemeris according to Farnocchia (2015)
[d] Scaled to a distance of 1 au.

as from the JPL final orbit reconstruction (Farnocchia, 2015). This orbital solution also provided us with the geometrical circumstances of solar illumination, through the phase angle $\phi = \widehat{\mathrm{OTS}}$, that is the angle at which the observer's (O) and Sun's (S) directions were seen from the target (T).

A different strategy was adopted during the entry phase of 2015 November 12-13, as the more favourable target magnitude allowed us to sample the luminosity trend on shorter timescales (down to 0.3 s in "quick-shot" R_c frames) in search for possible quick variability. A total of 98 magnitude estimates (65 R_c, 14 in V and B, and 5 in I_c bands) were collected, ending up with a final series of four 30 s R_c frames by letting the target trail across the field. These frames, between 05:07 and 05:16 UTC, that is just one hour before WT1190F atmosphere entry, allowed us to sample target luminosity on very short timescales (less than 0.2 s, see Sec. 4.1) such as to clearly detect and characterize the WT1190F spinning period. These observations are summarized in Table 2.

Using a subset of twelve frames with the best track-

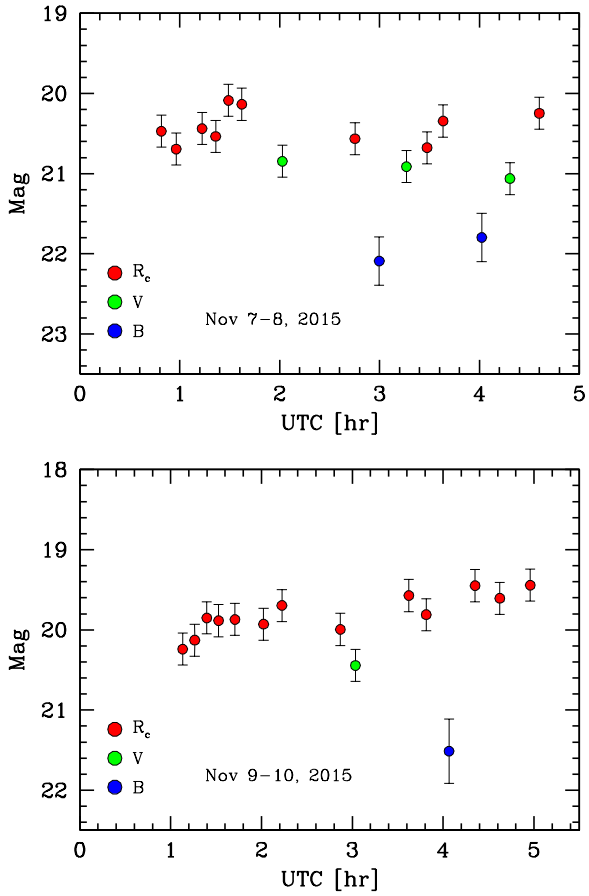

Figure 3: The WT1190F B, V, R lightcurve along the Loiano observing runs of 2015 November 7-8 and November 9-10. The x-axis timeline refers to the UTC hours respectively of Nov 8 and Nov 10.

ing quality and signal (these entries are marked with an asterisk in Table 1 and 2), we also obtained accurate astrometry of WT1190F, using the PPMXL catalog (Roeser et al., 2010) as astrometric reference. Since the reference stars were heavily trailed due to the non-sidereal tracking of the telescope, a trail-fitting procedure was used to determine their centroids. The resulting positions typically have an astrometric uncertainty of 0.2 arcsec, taking into account the contribution coming from the reference stars, the astrometric solution itself and the S/N ratio of the object (often very good). In addition, it is necessary to take into account a possible additional error source due to the camera timing, which thanks to some previous tests we conservatively estimate at about 0.2 seconds. This in turn converts into a variable astrometric error component given the object's angular speed, which is taken into account in all the subsequent analyses.

As a by-product, the astrometric procedure also provided further hints about the accuracy of the DASO magnitudes, by comparing, for instance, our twelve "astrometric" *bona fide* R mag estimates with the more accurate photometry presented here, as from Table 1 and 2. The mean magnitude residual, in the sense [DASO-current study],

Table 2: The Loiano observations of 2015 November 12-13

UTC[(a)] hh:mm:ss	Exp time [s]	Apparent mag	Band	log d[(b)] [km]	Absolute mag[(d)]	Phase[(c)] [deg]
		Nov 13, 2015 UTC				
00:22:35	420.0	16.38	R	4.902	32.75	65.8
00:27:41	60.0	16.31	R	4.897	32.70	65.9
00:29:21	30.0	16.26	R	4.896	32.66	65.9
00:30:37	30.0	16.30	R	4.895	32.70	66.0
00:32:03	30.0	16.77	V	4.893	33.18	66.0
00:33:14	30.0	16.82	V	4.892	33.23	66.1
00:34:54	60.0	17.67	B	4.891	34.09	66.1
00:38:21	180.0	17.66	B	4.887	34.10	66.2
00:41:44	120.0	17.57	B	4.884	34.02	66.3
00:44:01	30.0	16.75	V	4.882	33.22	66.3
00:45:18	30.0	16.18	R	4.881	32.65	66.4
00:46:27*	10.0	16.12	R	4.880	32.60	66.4
00:47:43	10.0	16.14	R	4.879	32.62	66.4
00:48:33	10.0	16.14	R	4.878	32.62	66.4
00:53:57	420.0	17.72	B	4.873	34.23	66.6
00:58:41*	3.0	17.62	B	4.868	34.16	66.7
01:00:17	3.0	16.14	R	4.866	32.68	66.8
01:01:37	1.0	15.94	R	4.865	32.49	66.8
01:03:23	2.0	15.97	R	4.863	32.53	66.8
01:05:34*	3.0	16.04	R	4.861	32.61	66.9
01:44:20	30.0	15.82	R	4.819	32.60	68.1
01:45:54	30.0	16.38	V	4.817	33.17	68.2
01:47:05	30.0	16.39	V	4.815	33.18	68.2
01:48:58	60.0	17.27	B	4.813	34.08	68.3
01:50:22	10.0	15.89	R	4.811	32.71	68.3
01:51:29	2.0	15.98	R	4.810	32.81	68.4
01:52:28	2.0	15.93	R	4.809	32.76	68.4
01:54:36	2.0	15.85	R	4.807	32.70	68.5
01:55:28	2.0	15.68	R	4.805	32.53	68.5
01:57:14	2.0	15.67	R	4.803	32.53	68.6
02:01:44	1.0	15.71	R	4.797	32.60	68.7
02:03:31	1.0	15.74	R	4.795	32.64	68.8
02:06:40	1.0	15.73	R	4.791	32.65	68.9
02:09:05	1.0	15.68	R	4.788	32.61	69.0
02:12:27	30.0	15.60	R	4.783	32.56	69.1
02:13:43	30.0	15.54	R	4.782	32.51	69.2
02:14:48	30.0	15.61	R	4.780	32.58	69.2
02:16:06	30.0	16.11	V	4.778	33.09	69.3
02:18:01	60.0	17.13	B	4.776	34.13	69.4
02:19:52	20.0	15.22	I	4.774	32.22	69.4
02:21:29	20.0	16.20	V	4.771	33.22	69.5
02:22:57	40.0	17.05	B	4.770	34.08	69.5
02:24:16	30.0	17.02	B	4.767	34.06	69.6
02:25:36	20.0	15.19	I	4.766	32.24	69.7
02:26:42	20.0	15.92	V	4.764	32.98	69.7
02:27:38	20.0	15.94	V	4.763	33.00	69.8
02:29:04*	1.0	15.52	R	4.760	32.60	69.8
02:30:17	1.0	15.30	R	4.758	32.38	69.9
02:34:20*	1.0	15.39	R	4.753	32.50	70.1
02:36:00	1.0	15.25	R	4.751	32.37	70.1
02:40:40	20.0	15.45	R	4.743	32.61	70.4
02:42:01	20.0	15.97	V	4.741	33.14	70.4
02:43:27	20.0	16.86	B	4.739	34.04	70.5
02:44:26	20.0	16.80	B	4.738	33.99	70.5
02:45:30	10.0	15.03	I	4.736	32.23	70.6
02:46:36	10.0	15.37	R	4.734	32.58	70.6
02:47:35	1.0	15.23	R	4.733	32.44	70.7
02:49:02	1.0	15.21	R	4.730	32.44	70.8
02:51:12	0.5	14.85	R	4.727	32.09	70.9
03:27:45	0.5	15.27	R	4.662	32.84	73.0
03:28:56	0.5	14.83	R	4.660	32.41	73.1
03:29:44	0.5	15.31	R	4.658	32.89	73.2
03:30:36	0.5	15.34	R	4.656	32.94	73.2
03:37:17	5.0	15.00	R	4.642	32.67	73.8
03:38:32	10.0	15.48	V	4.640	33.16	73.8
03:39:44	20.0	16.49	B	4.637	34.18	73.9
03:40:49	5.0	14.64	I	4.635	32.34	74.0
03:47:07	0.5	14.77	R	4.620	32.55	74.5
03:48:32	0.5	15.46	R	4.618	33.24	74.6
03:58:31	0.5	14.81	R	4.593	32.72	75.5
04:00:39	0.5	14.27	R	4.588	32.20	75.7
04:05:37	0.3	14.88	R	4.575	32.88	76.2
04:09:28	0.5	14.46	R	4.565	32.51	76.6
04:11:35*	0.3	13.79	R	4.559	31.87	76.9
04:14:53	0.3	14.60	R	4.550	32.73	77.2

Table 2 (continued)

UTC[a] hh:mm:ss	Exp time [sec]	Apparent mag	Band	log d[b] [km]	Absolute mag[d]	Phase[c] [deg]
04:19:22	0.3	14.38	R	4.537	32.57	77.8
04:21:17	0.3	14.47	R	4.530	32.70	78.0
04:24:07	5.0	14.21	R	4.521	32.48	78.4
04:25:06	5.0	13.89	I	4.518	32.17	78.5
04:26:21	5.0	14.71	V	4.515	33.01	78.7
04:27:33	5.0	15.40	B	4.511	33.72	78.8
04:28:57	5.0	14.05	R	4.507	32.39	79.0
04:30:03	5.0	13.78	I	4.502	32.15	79.2
04:31:01	5.0	14.75	V	4.499	33.14	79.4
04:32:06	5.0	15.56	B	4.496	33.96	79.5
04:34:00	0.3	14.69	R	4.488	33.13	79.8
04:55:22	1.0	14.26	R	4.406	33.11	83.7
04:56:29	0.3	14.61	R	4.400	33.48	84.0
04:57:26	0.5	14.10	R	4.396	33.00	84.2
04:58:40	0.5	14.24	R	4.392	33.16	84.4
05:00:33	0.5	13.48	R	4.381	32.45	84.9
05:06:01	10.0	13.60	R	4.352	32.71	86.5
05:07:28	30.0	13.65	R	4.346	32.79	86.8
05:08:39	30.0	13.88	R	4.339	33.06	87.2
05:09:34	30.0	13.88	R	4.334	33.08	87.4
05:12:05	30.0	13.69	R	4.318	32.97	88.3
05:13:10	30.0	13.57	R	4.313	32.88	88.6
05:14:41	30.0	13.63	R	4.306	32.97	89.0

[a] At mid exposure. Entries with asterisks have their astrometry published in the DASO Circ. (Altavilla et al., 2015).
[b] Target range according to Farnocchia (2015) final orbit reconstruction.
[c] Topocentric ephemeris according to Farnocchia (2015)
[d] Scaled to a distance of 1 au.

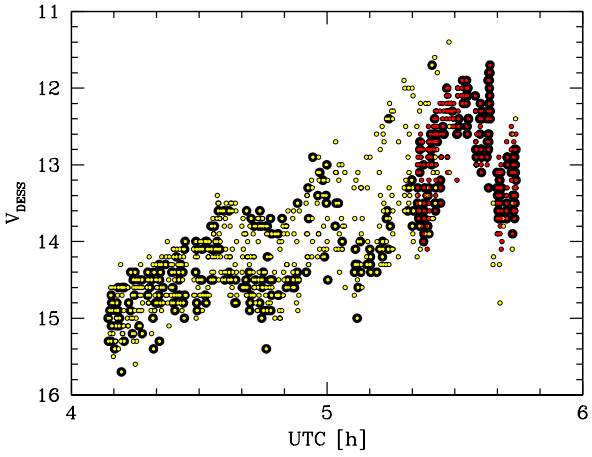

Figure 4: The full DeSS data set of 1125 V-band observations along the WT1190F final approach of 2015 November 12-13. The magnitude sample of the Tracker (yellow markers) and Antsy (red markers) telescopes (708 and 417 points, respectively) are merged in the plot, without relative offset correction. Bold points (for the two telescopes) refer to the astrometric DASO measurements (Sánchez-Ortiz et al., 2015). The x-axis timeline is in UTC hours of November 13.

results $\Delta R = -0.08 \pm 0.34$, a figure that may lead us to conclude that DASO magnitudes in Fig. 1 have a typical uncertainty of ± 0.3 mag.

2.1.1. Spectroscopy

Taking advantage of the "on-target" tracking capabilities of the telescope, a quite unique set of WT1190F low-resolution spectra were collected with BFOSC, between 03:07 and 03:23 UTC, that is about three hours before the final atmosphere entry, when the target was crossing the sky with an angular motion of some 250 arcmin hr^{-1}. In particular, two 300 s exposures have been carried out through a 5 arcsec-wide slit with the GR3 (blue) and GR5 (red) grisms. The grisms sampled the wavelength interval 3500-6000 Å with a 2.7 Å px^{-1} dispersion, and 5300-9500 Å with a 4.0 Å px^{-1} dispersion, respectively. With both grisms we secured a spectral resolving power, $R = \lambda/\Delta\lambda \sim 250$, leading to a 20 Å FWHM for the GR3 spectrum and 35 Å for the GR5 spectrum. Scientific target exposures were accompanied by the corresponding He-Ar frames for wavelength calibration, securing an accuracy better than $\sigma(\lambda) \leq 4$ Å. The instrumental response curve was finally recovered via past observation of the spectrophotometric standard star BD+28 4211 (Oke, 1990), observed with the same instrumental setup.

2.2. The Deimos DeSS dataset

Observations of WT1190F from the Deimos Sky Survey (DeSS) Observatory were especially focused to the night of November 12-13, to accurately track the body during its last hours in space. DeSS telescopes are located at Pico de Niefla, close to the Elecnor-Deimos premises in Puertollano (Castilla la Mancha, Spain), where they are remotely operated. Out of the three instruments currently active, mainly aimed at advanced SST observations of space debris and NEO objects, the two Tracker and Antsy telescopes joined for WT1190F observations.

Thanks to its higher sensitivity, with a 0.40m aperture and a f/9 Schmidt-Cassegrain optical design, the Tracker telescope delivered the bulk of target observations. The instrument was equipped with a 1024 × 1024 px CCD with 24 μm pixel size, covering a field of view of 20 × 20 arcminutes across the sky. Along the final leg of WT1190F approaching trajectory, the telescope was also flanked by the Antsy 0.28 m Rowe-Ackermann Schmidt astrograph, whose short focal ratio of f/2.2 provided a wider field of view of 1.3 × 1.3 deg. A 1024 × 1024 px back-illuminated EMCCD with 13 μm pixel size was attached to the camera. The extremely fast read-out capability of the detector allows the instrument to reach image rates of several frames per second, depending on binning and download mode. In addition, in its fast slewing mode, the Antsy telescope can track objects with exceptionally high angular motion, up to 6 deg s^{-1}.

Along the night, WT1190F was tracked from 04:08 UTC up to end of its visibility window, at November 13 sunrise. Over 1125 frames (708 with the Tracker telescope and 417 with the Antsy camera) were acquired, both for astrometric and photometric purposes (see Fig. 4). WT1190F was imaged, under photometric conditions, with typical exposures times between 5.0 and 0.1 s for Tracker frames and between 2.0 and 0.2 s for Antsy images (depending on target angular motion across the sky), which led to a S/N ratio better than 5 and 2, respectively. To improve target detection, both telescopes have been work-

ing in "white light", that is with no filters. However, instrumental magnitudes roughly matched Johnson V photometry as both CCD detectors happened to peak around 5500 Å, and WT1190F magnitude calibration relied on the surrounding grid of V reference stars across the observed field from the UCAC4 astrometric catalog (Zacharias et al., 2013). The full set of data is available to the interested reader upon request.

A comparison between TRACKER and ANTSY magnitudes in the common range of time (i.e. 05:21-05:44 UTC) shows that the latter ones tend to be brighter by $\Delta V = -0.22 \pm 0.74$ mag (in the sense [ANTSY-TRACKER]). On the other hand, a similar test of the TRACKER magnitude cloud around the timing of the last two V measurements from the Loiano dataset of Table 2 (i.e. between 04:26 and 04:31 UTC) indicates a photometric offset between the two V scales (in the sense [TRACKER-Loiano]), of $\Delta V = -0.32 \pm 0.35$ mag. When considering that the random scatter might likely be exacerbated by the quick intrinsic variability of the body (as we will see in Sec. 3.2 and 4.1) this figure closely recalls the typical DASO uncertainty discussed above. When merging the Loiano and DeSS photometric datasets, throughout the paper, we always applied these corrections.

For about one third (348 out of 1125) of the frames, an accurate astrometric measure of target position was also achieved, as published in the DASO database (Sánchez-Ortiz et al., 2015). Again, the UCAC4 astrometric catalog was taken as a reference for the calibration. Astrometry revealed to be a quite demanding task given the high angular motion of the body, especially in the very last moments of Earth approach, where the DeSS telescopes had to track at a speed of some 4000 arcmin h^{-1}. In addition, an accurate time tag is the mandatory requirement when carrying out astrometry at such extreme dynamical regimes. This is why we had to secure a clock accuracy better than 0.01 s in our observations, a figure well beyond the standard performance of more usual astronomic observations. Allover, our astrometric procedure secured for our DASO data an internal accuracy better than 1.0 and 2.5 arcsec for TRACKER and ANTSY, respectively.

3. WT1190F absolute magnitude

Relying on the DASO database to usefully complement our tuned observations we can now attempt a first in-depth overview of WT1190F's nature in terms of its apparent photometric properties. Two relevant parameters are to be dealt with, in this regard, as a minimal set to single out the physical signature of this body: these are the object's absolute magnitude and its possible variation law with the illumination phase angle.

From one hand, by converting apparent magnitudes to an absolute scale we can consistently compare target observations taken at different moments and different distance from us, thus rescaling the apparent flux to a fixed reference distance (conventionally set at 1 au). As is well known, this parameter is of paramount importance to constrain the object size. On the other hand, as both asteroids and man-made space probes actually shine by sunlight reflection, their photometric dependence on ϕ has evidently to relate to the target's geometry and physical composition.

3.1. Dependence on illumination phase angle

A total of 217 R-band DASO observations are available for WT1190F since its late-2015 (re-)discovery. An accurate orbit reconstruction has been possible for this period, that covers the last three orbits of the body, according to the JPL ephemeris (Farnocchia, 2015).

As these data came, however, from a coarse set of observatories worldwide, a statistical, yet effective, approach has been pursued to attach each observation an appropriate topocentric range distance and phase angle just relying on the *geocentric* JPL ephemeris. For this, one has to recall that, to catch WT1190F, each observer had to be located in the night-side of Earth (and therefore slightly *closer* to the target than the corresponding geocentric distance, when looking at convenient– say 30^o-40^o or better– zenithal angle). With little arithmetic, these simple arguments lead us to devise a straightforward correction scheme to the computed geocentric range distance ($d_{\rm geo}$) and phase angle ($\phi_{\rm geo}$). In particular, for each observing circumstance, WT1190F could be placed, on average, to a topocentric distance

$$d_{\rm top} \sim d_{\rm geo} - \frac{\sqrt{3}}{2} R_\oplus \tag{1}$$

(with $R_\oplus = 6367$ km the Earth's radius). From this distance the useful terrestrial cap, likely containing the observer, subtends an angle

$$\Delta\phi \leq \frac{R_\oplus}{2\, d_{\rm top}}. \tag{2}$$

The accuracy of our simplified scheme tends to increase with increasing target distance, and if we restrain to observations taken far enough (say for $d_{\rm geo} \geq 50\,000$ km), then we have, from eq. (2), that the geocentric phase angle ϕ actually approximates the true topocentric angle within a $\pm 4^o$ uncertainty. Accordingly, the absolute magnitude, as derived from eq. (1), carries an uncertainty of the order of or better than

$$\Delta mag \leq \pm 2 \frac{\Delta d}{d_{\rm top}} \sim \pm\sqrt{3} \frac{R_\oplus}{d_{\rm top}}, \tag{3}$$

that is a ± 0.2 mag figure, with our assumptions.

The resulting plot of the 190 relevant DASO data farther than the cut-off distance is displayed in Fig. 5. We also added to the plot the mean $R_c^{\rm abs}$ estimates from our Table 1 and 2 observations, as well as the mean magnitude estimate from the extensive survey of the G45 SST observatory. For the latter sample, we had to make Gunn r observations brighter by 0.35 mag to consistently match

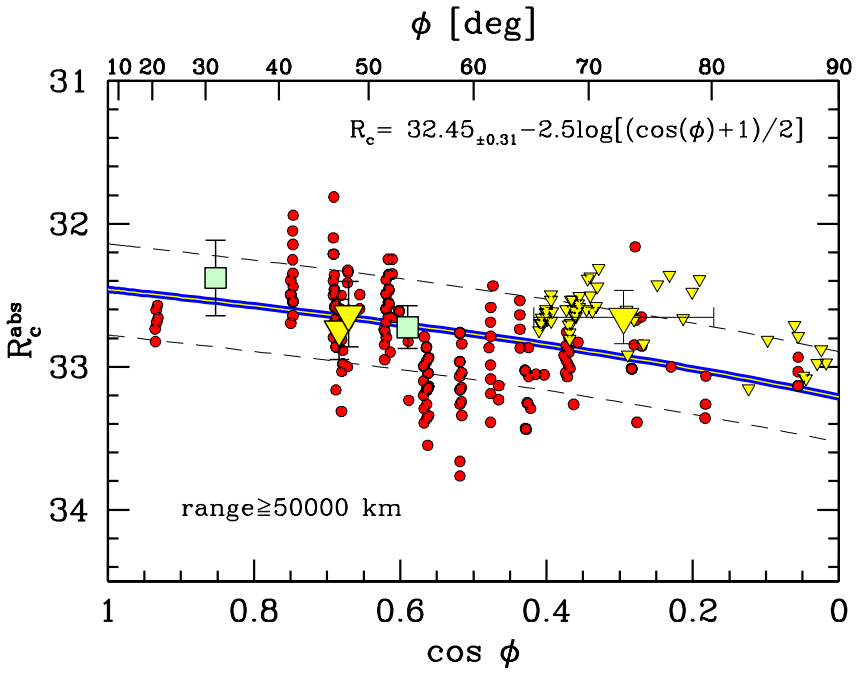

Figure 5: The WT1190F R absolute magnitude with changing orbital phase angle ϕ. The relevant DASO dataset of the 190 observations in year 2015 with geocentric distance in excess of 50 000 km is merged (red dots), after statistical correction, as explained in the text. These data are complemented by the Loiano observations of 2015 November (the three big triangle markers, as an average of each observing night), together with the individual measures of the November 12-13 approaching sequence (small yellow triangles). The G45 (SST Atom Site Obs.) Gunn r magnitude series are also joined, as an average for each observing night (big square markers) after correction to the Johnson-Cousins R band, as discussed in the text. The fitting curve, by assuming luminosity to be proportional to the target illuminated area, leads to an absolute magnitude of $R_c^{\rm abs} = 32.45_{\pm 0.31}$, as labeled in the plot.

the R_c scale. This offset was tuned up by means of a fit of the relevant $(R_c - r)$ versus $(V - R_c)$ empirical relationship for stars, as computed from the Vilnius spectral library of stellar types (Straizys & Sviderskiene, 1972).[3]

A first striking property that emerges from the plot is that WT1190F's brightness does not seem to vary so much with changing illumination conditions. A somewhat flat trend of $R_c^{\rm abs}$ with ϕ is evident, in fact, from the figure and, from a strictly statistical point of view, the rms scatter of the DASO points[4] ($\sigma \sim 0.29$ mag) may be fairly compatible even with a constant value of $R_c^{\rm abs}$. A more suitable alternative fit to the DASO data plus the November 12 Loiano observations (to better extend the ϕ coverage) could be attempted, suggesting a hint for R_c brightness to slighlty increase with decreasing ϕ. By assuming luminosity to be proportional to the target illuminated area (so that $L \propto [\cos\phi + 1]/2$) this leads to extrapolate[5] for WT1190F an absolute magnitude

$$R_c^{\rm abs} = 32.45_{\pm 0.31 (rms)} \qquad (4)$$

at $\phi = 0^o$. More generally, the lack of any evident surge effect when approaching "front-illuminated" configurations ($dR_c/d\phi \sim 0.007_{\pm 2}$ mag deg^{-1} from the data of Fig. 5) can be regarded as an important signature of the artificial origin of WT1190F. Man-made space artifacts, in fact, tend to level out their reflectance properties with changing phase angle, partly due to a smoother surface and to the averaging action of quick body spinning (e.g. Miles, 2011; Murtazov, 2013). Asteroids and the Moon, on the contray, likely display a much steeper trend $dR_c/d\phi \geq 0.03$ mag deg^{-1} (Li et al., 2015, see, e.g. Fig. 2 therein), and a stronger "opposition surge" in their reflectance when $\phi \to 0$ (Buratti et al., 1996; Nelson et al., 1998; Hapke & van Horn, 1963).

3.2. Magnitude variability

For its coarse nature, the full set of DASO observations does not allow any accurate assessment of WT1190F variability along its orbital path. Our Loiano observations of November 8 and 10 are the only explicit attempt in this sense, together with the 1004 r observations of October 25 by the G45 SST telescope at the Atom site (USA). The latter observations were taken under phase angle $\phi \sim 30^o \pm 2^o$

[3] The fitted relationship for stars is $(R_c - r) = 0.19\,(V - R_c) - 0.49$, which leads to $(R_c - r) \sim 0.35$ for moderately red objects, like WT1190F.

[4] The random scatter component of the magnitude sample is estimated by sorting points with increasing ϕ and then compute $\sigma^2 = \sum_2^n [mag_{(i)} - mag_{(i-1)}]^2/(n-1)$.

[5] Unfortunately, given the special WT1190F orbit configuration, small-ϕ geometries were only attained at unfavourable observing conditions, with the target in quick motion about its perigee. This prevented in Fig. 5 any fair sampling of WT1190F under "front-illuminated" situations.

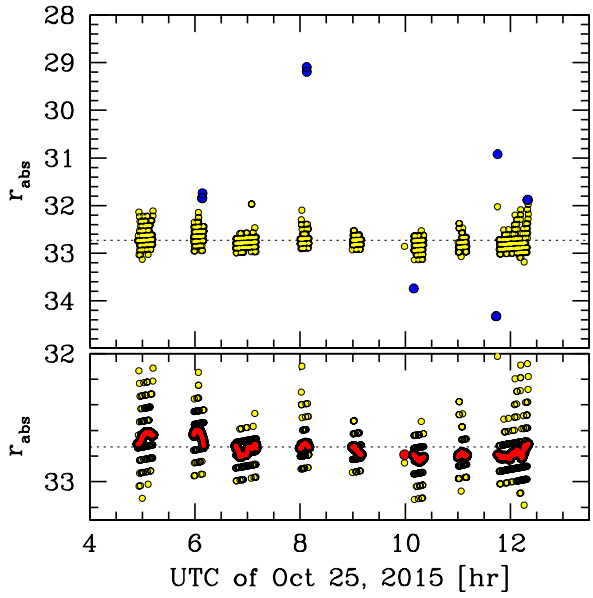

Figure 6: The 1004 Gunn r observations of 2015 October 25 by the G45 SST telescope at the Atom Site Obs. (USA) are displayed, after correcting for distance to an absolute magnitude scale. Interloping the quiescent underlying behaviour of WT1190F (yellow dots), one can recognize in the upper panel a remarkable series of flares and dimming events (blue dots), on timescales of seconds, exceeding a 3σ random fluctuation around the average magnitude of the data. Besides this abrupt and striking variation, the G45 data do not show any sign of coherent trend on slower timescales, as shown by the smoothing running average (red dots) displayed in the zoomed in point distribution of the lower panel.

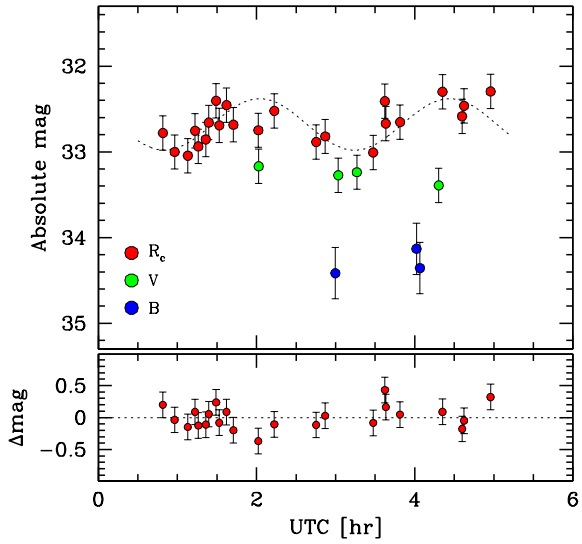

Figure 7: The Loiano observations of Fig. 3 are merged in the upper plot, after rescaling to absolute magnitudes. The displayed pattern in both 2015 November nights for the WT1190F R magnitude to change on a tentative timescale of 2.4 hours is reinforced here, as a (somewhat speculative) evidence of a coherent object variability with an amplitude of about 0.7 mag (dotted curve). The magnitude residuals with respect to a fitting sinusoidal curve have a $\sigma_R = 0.18$ mag (rms) and are displayed in the lower panel. See text for a discussion.

while from Loiano we have been probing the angular range $\phi \sim 47^o \pm 1^o$.

The G45 lightcurve is reported, with different scales, in the two panels of Fig. 6. Its random point scatter of $\sigma \sim 0.29$ mag may easily hide any inherent variability of the object of the same order of amplitude. Interestingly enough, however, in the upper panel of the figure a remarkable series of flares exceeding a 3σ random fluctuation, with at least four relevant events of straight brightening around 6^h, 8^h and 12^h UTC, and two less pronounced dimming events, around 10^h and 11.5^h UTC. Although part of the brightening spikes may be due to spurious blends of the target with overlapping stars, if we consider the sampling frequency of G45 observations (about one frame every 8 seconds), this leads to conclude that WT1190F may have likely varied on shorter timescales, probably in consequence of some mirroring facets of a spinning body. We will return in better detail on this issue in the next section.

In order to probe variability on longer time periods, we smoothed the G45 observations by an 80-points running average to improve the photometric accuracy, still attaining roughly a 10-min time resolution, as shown in the zoomed panel of Fig. 6. This procedure actually allowed us to detect some coarse pattern in WT1190F luminosity along the night, although no conclusive evidence for any periodicity of the data can be achieved.

A slightly cleaner photometric signature is present, on the contrary from the Loiano observations of November 8 and 10, especially when focussing on the R_c lightcurve in the two panels of Fig. 3. One may in fact tentatively recognize a similar magnitude pattern that replies in both nights, suggestive of a raising luminosity straight at the beginning and end of the observations, and a relative magnitude dip around 3^h UTC. When rescaling for distance and merging the data of the two nights, as in Fig. 7, the pattern reinforces slightly more, and suggests a variability over a time frequency of coincidentally 9 or 10 periods per day (namely a period of 2.7 or 2.4 hours, respectively). One has to stress, however, the somewhat speculative nature of this result, as the improvement of the statistical point rms, for instance around a sinusoidal lightcurve as in the figure, is admittedly only a marginal one ($\sigma_R = 0.18$ versus 0.22 mag) with respect to the scatter around a flat value of $\langle R_c \rangle$.

The lack of any supporting evidence from the G45 observations may not, by itself, rule out this hypothesis. In fact, a phase angle difference of almost 20^o between the two data sets may account for a substantial difference in the reflecting surfaces of the body, especially if WT1190F were most likely orbiting with "inertial actitude" orientation, that is by facing a fixed direction with respect to the celestial reference framework (and not with respect to Earth).

4. The Earth final approach and atmosphere entry

For its special relevance, the WT1190F entry event of 2015 November 13 (UTC) worths a specific discussion. According to the JPL final orbit reconstrucition (Farnocchia, 2015), the highly elliptical orbit led the object to head Earth with a steep incidence angle and with a relative velocity very close to the escape limit. To all extent, therefore, the dynamical characteristic of the event closely mimicked an asteroid impact of deep-space origin.

Given the favouring location, close to Earth's terminator at the daylight time of WT1190F entry over Sri Lanka, the Loiano and Mt. Niefla DeSS observatories were the only professional ones that have been able to track the object in its final orbital leg. In particular, from Loiano we caught WT1190F at a range distance of 80 000 km, leaving the target at 05:14 UTC (see Table 2), at a distance of 20 200 km. An even better score was achieved by the Mt. Niefla telescopes, which docked WT1190F 38 000 km away up to 05:44 UTC, when the target was at a distance of only 12 500 km (and an altitude of 11,400 km), about 34 minutes before the atmosphere entry. The DeSS observations are the latest ones available for WT1190F.

The BVR_cI_c multicolor photometry of WT1190F, from Loiano, is displayed in the upper panel of Fig. 8. As a range of different exposure times, as short as 0.3 s, were adopted according to Table 2, in the plot we merged adjacent "quick-shot" exposures such as to reach a minimum integrated time of 1 sec. This left us with 78 displayed points out of the 98 total magnitude estimates. A quick increase of target apparent luminosity is evident from the figure, as the distance to Earth steadily decreased. Once recovering for the range distance and rescaling to absolute magnitudes (mid panel of the figure), the trend greatly flattens pointing to an almost constant value, though still with a residual tendency for the object to slightly brighten (intrinsically) along the night. The nominal fit of the data versus time provides,

$$\left.\begin{array}{rcll} B^{\rm abs} & = & -0.053_{\pm 0.021}t + 34.18_{\pm 0.05} & 0.09\,{\rm mag(RMS)} \\ V^{\rm abs} & = & -0.034_{\pm 0.017}t + 33.21_{\pm 0.05} & 0.07\,{\rm mag(RMS)} \\ R_c^{\rm abs} & = & -0.033_{\pm 0.017}t + 32.67_{\pm 0.04} & 0.12\,{\rm mag(RMS)} \\ I_c^{\rm abs} & = & -0.023_{\pm 0.032}t + 32.30_{\pm 0.11} & 0.06\,{\rm mag(RMS)}, \end{array}\right\} \quad (5)$$

with t in UTC hours.

We are inclined to attribute such a small magnitude trend to the effect of Earth illumination as the target approached our planet hovering the daylight hemisphere. The order of magnitude of this brightening depends, of course, on Earth albedo and target altitude, and simply derives from the energetic budget of the incident flux ($f_{\rm in}$) on the object. In the Earth's vicinity, the latter can be written as

$$f_{\rm in} = f_\odot + f_\odot \frac{\alpha_\oplus A}{4\pi h^2} \leq f_\odot \left[1 + \alpha_\oplus \left(\frac{R_\oplus}{h}\right)^2\right] \quad (6)$$

where $f_\odot$ is the solar flux at Earth, $\alpha_\oplus$ is the Bond albedo of our planet, A and $R_\oplus$ are, respectively, the illuminating area and the Earth's radius, and h the target altitude (from Earth's surface). In terms of magnitudes, the target extra-luminosity provided by Earth illumination should therefore be of the order of

$$\Delta mag \leq \frac{\alpha_\oplus}{h_\oplus^2}, \quad (7)$$

provided to express the target altitude $h_\oplus$ in units of Earth's radius. As $\alpha_\oplus \sim 0.3$, the expected brightening quickly vanishes with increasing $h_\oplus$ but as close as, say, $3R_\oplus$ it can raise up to 0.03 mag. Although in the correct way, this effect could however only partially account for the observed trend, as the set of eq. (5) points to a change of about 0.15 mag along the observing run. Quite interestingly, this apparent discrepancy may actually indicate that WT1190F was indeed *mirroring* (rather than *scattering*) Earth's daylight flux.

In the previous fit of Fig. 8 data we left aside the very last group of R_c observations (later than 04:40 UTC, which

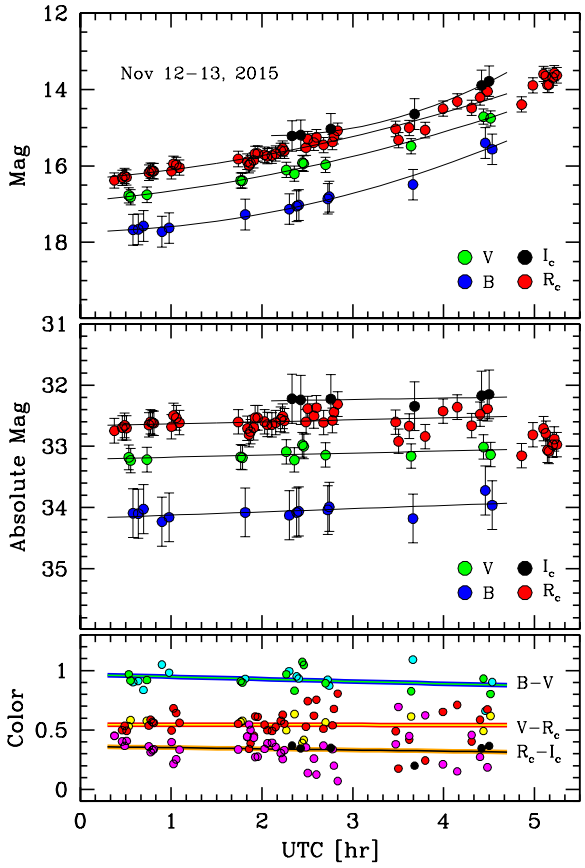

Figure 8: The B, V, R_c, I_c photometry of WT1190F during its final Earth approach of 2015 November 12-13, as seen from Loiano, are reported in the upper panel. Once rescaling for the (quickly reducing) distance, the inferred absolute magnitudes and colors are shown, along the same night, in the mid and lower panels of the figure, respectively. The fit of these data is reported in the set of eq. (5) relations. Note the abrupt drop in object's R-band absolute luminosity about 05:00 UTC (as in mid panel). The x-axis timeline in the figure is in UTC hours of Nov 13.

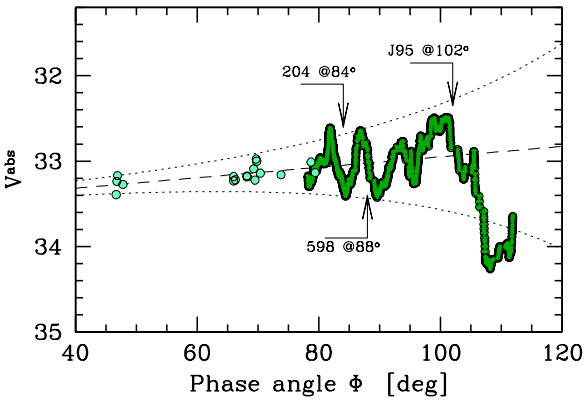

Figure 9: The absolute V-band magnitude trend with orbital phase angle ϕ along the final approaching trajectory of WT1190F. The Nov 12-13 DeSS observations (green solid curve), for $\phi > 78^o$ are merged with the Loiano coarser set of measures, sampling lower phase-angle figures. Note the diverging oscillating regime of WT1190F luminosity on $\sim$ 20 min timescales, that abruptly sets in place with ϕ approaching and exceeding a square-angle illumination aspect. To better single out the trend, DeSS data have been smoothed with a 30-point running average. As discussed in the text, in their comparison with the Loiano dataset, both TRACKER and ANTSY magnitudes have been corrected accordingly. The relevant timing of Campo dei Fiori (code "204"), Loiano ("598") and Great Shefford ("J95") lightcurve sampling of Fig. 11 is marked on the plot.

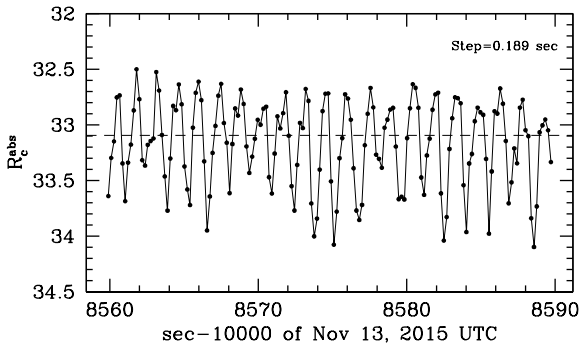

Figure 10: The quick variability of WT1190F clearly appears in this R-band trailing frame from Loiano, taken at 05:09:34 UTC of 2015 November 13 (see Table 2). A total of 21 pulses can easily be recognized in the figure, suggestive of a flashing period slightly shorter than 1.5 s. The time span of target trail across the CCD pixels, for this frame, is 0.189 s px^{-1}.

clearly show an intervening change in WT1190F photometric behaviour, with a noticeable and abrupt dimming of the absolute magnitude. The entangled pattern becomes actually even clearer in Fig. 9, when merging the Loiano and DeSS V-band observations versus the appropriate topocentric phase angle (as from the JPL data). To gain a better view of the general trend, in the figure we smoothed the DeSS data with a 30-point running average, degrading the time resolution to roughly 2 min.

The figure shows that, beyond a phase angle of $\sim 80^o$, WT1190F luminosity entered a diverging oscillating regime roughly on a 20 min timescale, that reached an amplitude of up to one magnitude in the very late stage before the atmosphere entry. Note that this oscillation is not evident, for instance, in the earlier R-band observing sequence of Fig. 8 (mid panel). Quite interestingly, such a wild photometric behaviour keeps growing when ϕ approaches and exceeds a square angle, that is when the Sun begins to illuminate the target "from behind".

4.1. WT1190F spinning properties

The enhanced apparent luminosity of WT1190F during its final approaching trajectory made possible a unique investigation of its short-timescale variability. The quick magnitude change escaped, in fact, any previous detection along the whole observing timeline, back from year 2009, as the body never approached by less than 20 000 km at its perigee crossing. From one hand, at this distance its apparent magnitude was still too faint for rapid photometry with most small amateur telescopes; on the other hand, the exceedingly high angular motion made the body too fast to be successfully tracked with bigger professional telescopes.

A direct evidence for a flashing behaviour of WT1190F just appeared in the final images from Loiano, where the target was left trailing across the CCD field. An example of the resulting lightcurve, for the 05:09:34 UTC frame of Table 2, is displayed in Fig. 10. During the 30 s exposure the object slightly moved across the CCD pixels thus allowing us to sample the WT1190F lightcurve with a time resolution $\delta t \sim 0.189$ sec px^{-1}. A total of 21 pulses can easily be recognized in the figure, a variability pattern that has been replying in all the trailing R_c frames, spanning a total time baseline of about 7 min (roughly 300 duty cycles), with the target illuminated at a phase angle $\phi \sim 88^o \pm 1^o$. This feature immediately calls for a flashing period slightly shorter than 1.5 s.

Our rough estimate can however be further refined thanks to a much larger time baseline of the DeSS data (about 100 min in total), in particular with the TRACKER telescope. Just restraining to the first burst of 567 observations, taken at orbital phase angle $\phi \leq 90^o$, we lead to a best estimate of the flashing period of

$$P_{\rm flash} = 1.4547_{\pm 0.0005}\,{\rm s}. \quad (8)$$

The mean lightcurve stemming from the relevant DeSS data is displayed in the lower panel of Fig. 11.[6] When phased together with the same period, the Loiano trailing data also nicely confirm the same pattern (mid panel of Fig. 11), with a variability amplitude about 1.1 mag.[7]

[6] One has to remark that the flashing period of eq. (8) is the *apparent*, not the *inertial* one. For the latter, the exact inertial orientation of WT1190F must have been known.

[7] The real variability amplitude depends on the mean time resolution, δt, of the single magnitude points. This is either the mean exposure time for the DeSS data or the sampled time-per-pixel value for the Loiano trailing images. The value of δt works as a smoothing

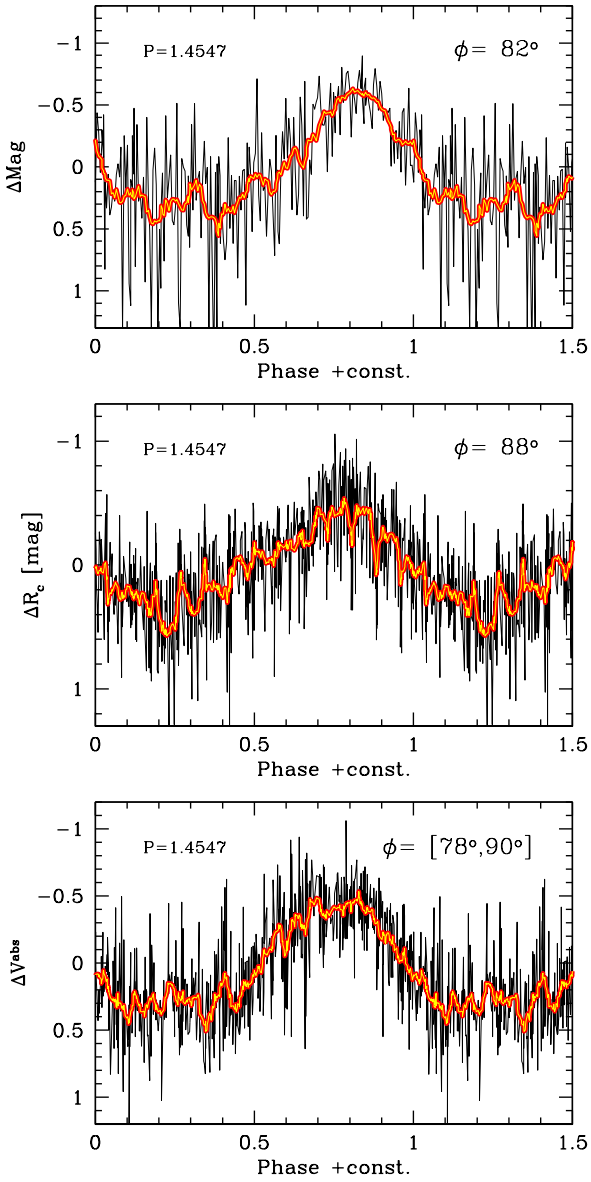

Figure 11: The WT1190F lightcurve by phasing observations with the short "flashing" period of eq. (8). The three different datasets of Buzzi & Colombo (2015, Campo dei Fiori Obs.; upper panel), Loiano (mid panel) and DeSS (Tracker telescope; lower panel) are displayed, for comparison. For a better reading, the raw data distribution is smoothed with a 15-point running average (thick solid line). The geometrical circumstance of the orbital phase angle ϕ spanned by the observations is reported top right in each panel.

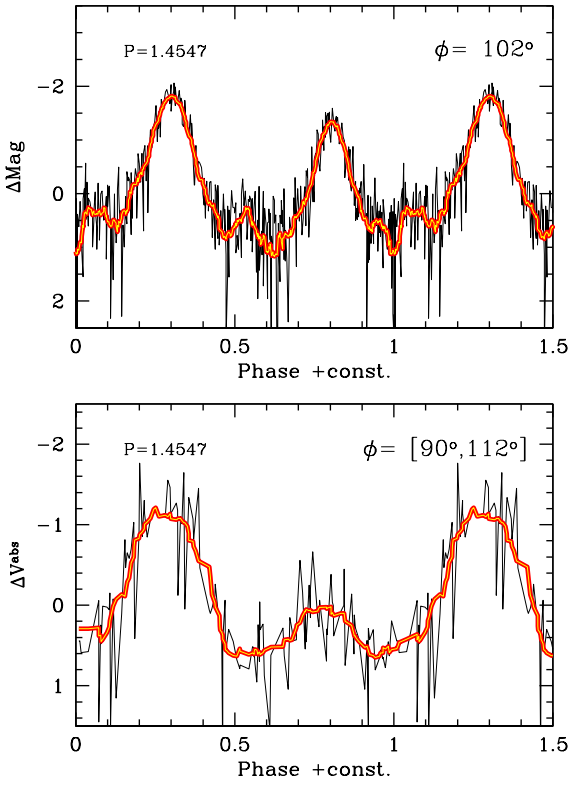

Figure 12: Same as Fig. 11, but for two datasets taken at orbital phase angles larger than 90^o, namely the Birtwhistle (2015) data taken at Great Shefford Obs. (upper panel) and the DeSS data (Tracker telescope; lower panel). Compared to the previous figure, a substantial change in the lightcurve shape is evident, with an intervening secondary maximum that keeps growing midway of the curve. This transient feature (that only appeared in the very last minutes before the atmosphere entry of WT1190F) is striking in the Great Shefford data and found full confirmation from the DeSS observations.

Minutes before the Loiano observations, the amateur observatory "G. Schiaparelli" of Campo dei Fiori (Italy, with code "204") was able to detect WT1190F variability in a series of CCD images (Buzzi & Colombo, 2015) taken between 03:29 and 04:29 UTC, with the target illuminated under a phase angle $\phi \sim 82^o$. According to the published frames, we computed the mean lightcurve, displayed here in the upper panel of Fig. 11. The Buzzi & Colombo (2015) observations fully confirm our results, suggesting also in this case a magnitude amplitude of 1.2 mag, with a time resolution $\delta t \sim 0.132$ s.

A further important contribution also came from the Great Shefford Obs. (in UK, with code J95, Birtwhistle, 2015), where one trailing image, taken at 05:34:38 UTC, about a phase angle $\phi \sim 102^o$, clearly shows a more entangled pattern for WT1190F with a double-peaked magnitude variation pointing to a period of some 0.73 sec, just half our flashing period. Relying on the published frame, we computed the mean lightcurve by phasing the data with the eq. (8) period. The result of our image processing is shown, for comparison, in the upper panel of Fig. 12.

Admittedly, the J95 observations add a puzzling piece of information to our analysis and possibly a crucial constraint to the inferred geometric configuration of WT1190F. Contrary to the previous lightcurves (for $\phi \leq 90^o$), the Birtwhistle (2015) observations show a much larger variability, up to a 3.0 mag amplitude. This seems to be an

parameter for the lightcurve. Evidently, a shorter value assures a more resolved curve, and a less biased estimate of the inherent amplitude of the magnitude variation. For the DeSS data $\delta t \sim 0.5$ s, while for Loiano $\delta t \sim 0.196$ s.

intrinsic feature of the curve, certainly secured by a fairly better time resolution ($\delta t \sim 0.051$ sec) compared to the other cases. In closer analysis, however, even the Great Shefford data do actually confirm our period estimate, as the "half-period peak" appears in fact to be a secondary maximum of lesser strength, abruptly grown midway along the curve when ϕ exceeds 90^o and the Sun keeps illuminating "from behind". This key piece of information still seems to unambigously emerge from the DeSS data, when restraining to our latest TRACKER observations, for $\phi > 90^o$ (as compared in the lower panel of Fig. 12). The observed amplitude, in this case is just about 1.9 mag, due to a coarser time resolution of the data.

The combined analysis of Fig. 9, 11 and 12 lightcurves greatly helps clarifying the exact evolution of the WT1190F luminosity with changing the illumination geometry and, by relying on simple geometric arguments of symmetry, this leads us to the conclusion that WT1190F was in fact consisting of *four* mirroring facets (roughly at orthogonal directions), therefore pointing to a physical spinning period for the body of twice the nominal duty cycle, that is

$$P_{\rm spin} = 2.9094_{\pm 0.0003}\,{\rm s}. \quad (9)$$

4.2. The atmosphere entry trajectory

An accurate observation of the WT1190F atmosphere entry has been carried out on 2015 November 13, by an international airborne mission sponsored by the United Arab Emirates (UAE) Space Agency and the International Astronomical Center (IAC) in Abu Dhabi (Jenniskens et al., 2016). The target was successfully tracked with optical and NIR detectors, leading to estimate its temperature and absolute magnitude during the fireball phase across the atmosphere.

The steep incident angle ($\sim 20^o$) and the hypersonic velocity (10.6 km s^{-1}) led WT1190F to enter the atmosphere at a vertical speed of ~ 3.6 km s^{-1}, which greatly reduced the total crossing time, when compared to standard reentry scenarios as from LEO objects. In particular, the crucial fireball phase, between a quote of 80 and 40 km, was accomplished in some 11 seconds. In this timescale, WT1190F had to release just twice the amount of kinetic energy of a corresponding LEO body, reaching a factor of $2^{1/4} \sim 20\%$ hotter temperature. For the latter, the Jenniskens et al. (2016) airborne spectroscopic observations suggest that $T \sim 3000$ K was eventually reached during the entry trajectory. This figure is close, but slightly lower than the Titanium evaporation point.

Our processing of the published co-added image,[8] which traces the full WT1190F burning trajectory is displayed in Fig. 13. According to the Jenniskens et al. (2016) calibration (see Fig. 5 therein), the target became visible at a height of 73 km, peaked in luminosity about 50.5 ± 2.5 km,

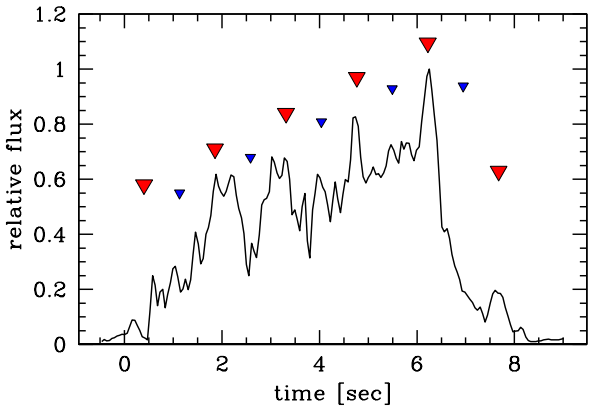

Figure 13: The apparent luminosity of WT1190F during its atmosphere burning phase, according to the Jenniskens et al. (2016) observations. At the timeline origin of the plot, the object started to brighten at a height of 73 km reaching a maximum peak luminosity 6.3 s later, about 50.5 ± 2.5 km. Notice the flashing behaviour along the atmosphere entry, which seems to be consistent with eq. (8) (primary and secondary peaks, as from Fig. 12, are sketched respectively by red and blue triangles along the curve).

and then quickly faded. A multiple (non-explosive) fragmentation started just before the main luminosity peak and continued down to a height of 30 km eventually leaving the body broken into up to 18 pieces. In detail, Fig. 13 may suggest that, along the fiery entry, WT1190F likely continued to spin (Jenniskens et al., 2016). This feature, together with the reduced burning time, may have partly shielded even more vulnerable structures of the body. As a consequence, possibly a large fraction of WT1190F could have survived the entry event.

A further consequence of the WT1190F steep entry angle is that the path of its fragmented debris should have not so much departed from the straight ballistic trajectory, thus making the landing spot much smaller than a corresponding LEO case.

The bathimetric map of Fig. 14 may help, in this regard to better locate the position of the possible survived debris, off the coast of Sri Lanka. In the figure we superposed the WT1190F nominal trajectory, according to the JPL model, to the sea floor measurement grid of the National Centers of Environmental Information of the NOAA (USA).[9] The WT1190F track starts at an altitude of 100 km, with the target arriving from the West down to the impact point. Labelled on the plot are the ballistic reference altitude (in kilometers) and the underlying sea depth (in meters).

4.2.1. Assessing the impact point accuracy

Quite interestingly, the accurate post-entry reconstruction data of Farnocchia (2015), relying on the full DASO astrometric database, provide us with a solid reference framework to quantitatively assess the real capabilities of

[8] Publicly available at the URL: *http://impact.seti.org*. See also Fig. 4 of Jenniskens et al. (2016).

[9] An interactive map viewer is on line at the URL: *https://maps.ngdc.noaa.gov/viewers/bathymetry*.

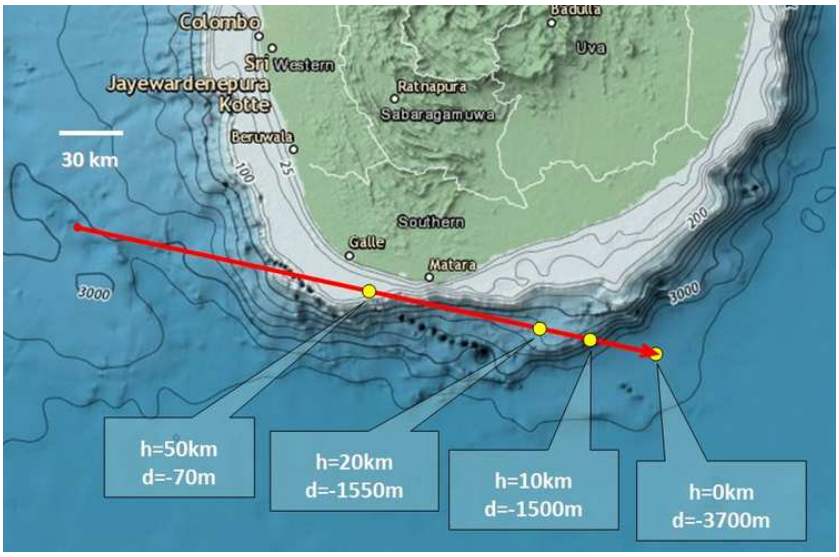

Figure 14: The WT1190F entry trajectory superposed to the bathimetric map of Sri Lanka offshore, according to National Centers of Environmental Information of the NOAA (USA). Labelled on the plot are the ballistic reference altitude (in kilometers) and the underlying sea depth (in meters) at some reference points along the trajectory. See text for full discussion.

a reduced set of observing stations, like the Loiano and the DeSS telescopes, to effectively constrain the trajectory in the event of a deep-space impactor like WT1190F.

For our excercise, we first considered the case of the Loiano astrometric data alone, just relying on the DASO subsample of Table 1 and 2 data (those entries marked with an asterisk in the tables). As a second step, to this minimal dataset (though spanning a large orbital arc) we then added the denser DASO astrometry set of DeSS observations, which better spotted the final leg of the orbit. In order to evaluate the actual uncertainties from a purely dynamical perspective, the discussion below only refers to the plain ballistic trajectory, without taking into account any drift caused by the interaction with the atmosphere. Our calculations were carried out with the FIND_ORB software[10]

The Loiano-only dataset is sufficient to predict the impact point with a formal spatial accuracy of ±600 m, mostly along the direction of motion; the time of impact is known to about 1 seconds at the 1-sigma level. With the addition of the DeSS data, the precision of the impact location further improves to about ±400 m, while the time of impact can now be constrained to about 0.1 s. These precision estimates are quite robust to small changes of the astrometric assumptions (timing and astrometric error bars).

As a final step of our analysis, the full impact trajectory computed from our datasets can be compared with the Farnocchia (2015) JPL orbital solution, which includes post-entry reconstruction data and can therefore be assumed as a "ground truth" to estimate the accuracy of our approach. The agreement between the two is superb: for both the Loiano-only and the Loiano+DeSS datasets, our trajectory is spatially within 300 meters from the actual one, and the timing offset is less than 0.1 s for the Loiano data, and about 0.01 s for the two-stations solution.

All the estimates presented here are based on a dynamical model that includes not just gravity, but also the perturbing effects of solar radiation pressure (SRP) on the object's trajectory. The SRP effect is modeled under the assumption that the body behaves as a spherical absorber, although for an artificial object this assumption may be oversimplified. A full discussion of the importance of the SRP parameterization, and of the area to mass ratio derived from it, for the object identification is presented in Sec. 6.2; from a purely dynamical perspective, it is however important to point out that, without at least a simple modeling of this non-gravitational force, any observations fit for arcs longer than a few days would show unphysical residuals for the observations. Those would in turn lead to a shift of the predicted trajectory that even for the short arc used in this analysis would have been larger than the error bars of the solution.

The achieved accuracy in the trajectory definition is so good that it is not unreasonable to consider it as a valuable guidance in case a future submarine mission ever attempts to recover the WT1190F wreck. Taking again the bathimetric map of Fig. 14 as a reference, a straight ballistic trajectory, without any interaction with the atmosphere, would have resulted in an impact with the ocean surface at 5.6299^o N, 81.4898^o E, where the seabed is extremely deep, being located about 3700 m under the surface. According to previous arguments, however, as the object fragmented earlier, then the surviving debris might now be underwater much closer to the Sri Lanka coast,

[10]The programme is publicly available at the URL: *http://www.projectpluto.com/find_orb.htm*.

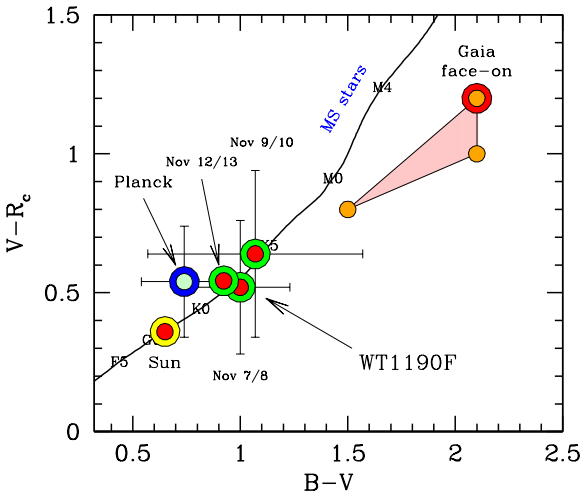

Figure 15: The $(B-V)$ versus $(V-R_c)$ average colors of WT1190F along the three observing runs of 2015 November, from Loiano. The target colors are compared with other reference objects, namely the Planck and Gaia spacecraft, the Sun, and the locus of Main Sequence stars, according to the Pecaut & Mamajek (2013) calibration (solid curve, labeled with the stellar spectral type). WT1190F appears to be slightly "redder" than the Sun, but very close in color to Planck. It would also quite well match the colors of a star of spectral type K3.

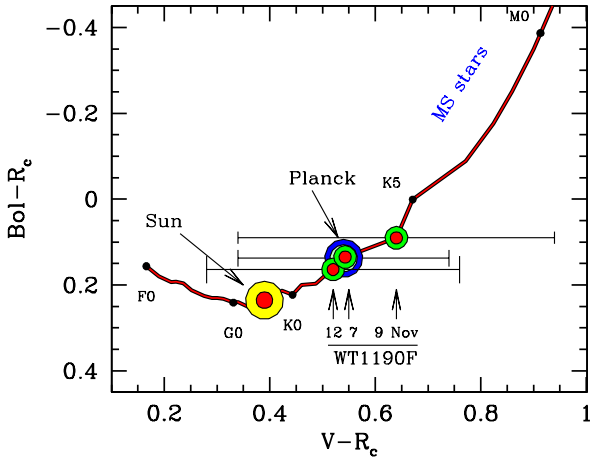

Figure 16: The reference framework of Fig. 15 is replied here to assess the bolometric correction to the R_c band. The average $(V-R_c)$ color of WT1190F along the three observing nights of 2015 November intercepts the Pecaut & Mamajek (2013) stellar calibration to derive a confident estimate of the bolometric correction about $(Bol-R_c) \sim 0.13_{\pm 0.05}$ mag. Note, again, the close match of WT1190F with the the Planck deep-space probe.

along a quite tight strip (well less than 1 km wide) within $[30\ \mathrm{km}/\tan(20^o)] \sim 80$ km before the nominal ballistic impact point, at a depth of some 1500 meters or even shallower. Perhaps two thirds of the WT1190F mass could be hidden there (Jenniskens et al., 2016).

5. Spectral energy distribution and reflectance properties

The Loiano observations provide a unique dataset to probe the WT1190F SED. The extensive BVR_cI_c multicolor photometry, complemented by the low-resolution spectra, taken three hours before the atmosphere fiery entry, may supply important clues to shed light on the target physical composition, through an accurate sampling of its reflectance curve between 4000 and 9000 Å.

5.1. Colors and bolometric correction

A first estimate of the target colors can be done from the data of Table 1, where we just averaged the R_c magnitudes to match the few B and V observations. A more elaborated analysis can be carried out, on the contrary, for the night of November 12-13, where Fig. 8 and the set of eq. (5) lead to a much firmer estimate of the apparent flux in the different photometric bands. We summarized in Table 3 our results for the three observing nights of 2015 November.

In spite of any change of the phase angle, one sees from the table that WT1190F did not display any appreciable variation in its apparent colors along the full orbit, from translunar distances down to Earth. When compared, in Fig. 15, with the $(B-V)$ versus $(V-R_c)$ colors of other relevant deep-space spacecraft, like the L2 probes Planck and Gaia (Buzzoni et al., 2016), and with the stellar locus of Main Sequence stars of different spectral type (as from the Pecaut & Mamajek, 2013, compilation), WT1190F was slightly "redder" than the Sun, but substantially "bluer" than Gaia, and close to the colors of the Planck spacecraft. According to the figure, the target quite well matches also the stellar locus, being consistent in color with a star of spectral type K3.

Table 3: The WT1190F observed colors

Night date UTC	ϕ [deg]	R_c^{abs}	B-V	V-R_c	R_c-I_c
Nov 8, 2015	46.9	$32.74_{\pm 0.21}$	$1.00_{\pm 0.23}$	$0.52_{\pm 0.24}$	
Nov 10, 2015	47.9	$32.63_{\pm 0.23}$	$1.07_{\pm 0.5}$	$0.64_{\pm 0.3}$	
Nov 13, 2015	72.9	$32.65_{\pm 0.19}$	$0.92_{\pm 0.03}$	$0.54_{\pm 0.01}$	$0.33_{\pm 0.02}$

By relying on the stellar calibration we can also suitably convert WT1190F broad-band magnitudes into a bolometric scale, the latter far more effective to self-consistently assess the inherent emitting properties of the body, as we will see in the next section. A bolometric correction to the R_c band easily derives from the Pecaut & Mamajek (2013) $(Bol-R_c)$ versus $(V-R_c)$ color relationship, as displayed in Fig. 16. In the figure we also located the Sun and the Planck probe[11]. In the WT1190F color range, a consistent correction of

$$Bol - R_c = +0.13_{\pm 0.05} \quad \mathrm{mag} \tag{10}$$

is envisaged. In addition, taking the November 13 mean

[11] Due to its exceedingly "red" color, Gaia lies, on the contrary, well off the plot at a much higher bolometric correction (Buzzoni et al., 2016)

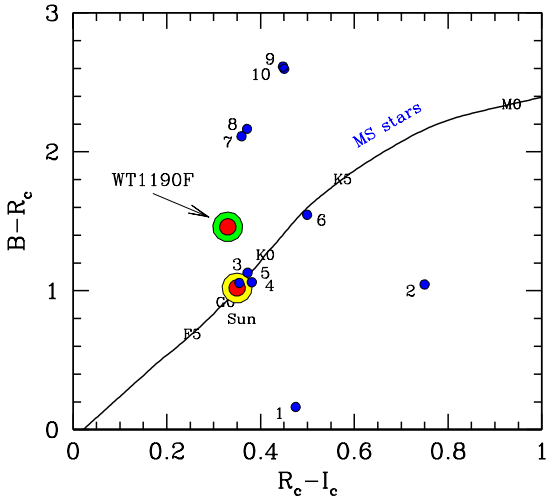

Figure 17: The WT1190F location in the $(R_c - I_c)$ versus $(B - R_c)$ color domain, according to the Loiano observations of 2015 November 12-13. Compared with the Pecaut & Mamajek (2013) stellar locus, the object appears now with an exceedingly "blue" $(R_c - I_c)$ color, suggestive of a reduced reflectance in the I_c band. To further investigate this feature, we also report in the plot the expected colors for different materials extensively used in spacecraft and rocket assembly, as from the Cowardin (2010a) and Cowardin et al. (2010b) lab measurements. The point caption is: 1 = GaAs solar panel; 2 = std solar panel; 3 = Impacted MLI (Al+Cu Kapton sandwitched with beta cloth substitute); 4 = Al Kapton (inner side facing spacecraft); 5 = Al Kapton (outer side facing space); 6 = Mylar; 7 = Al backing solar cell (facing space); 8 = Cu Kapton (facing space); 9 = Al backing solar cell (facing spacecraft); 10 = Cu Kapton (facing spacecraft).

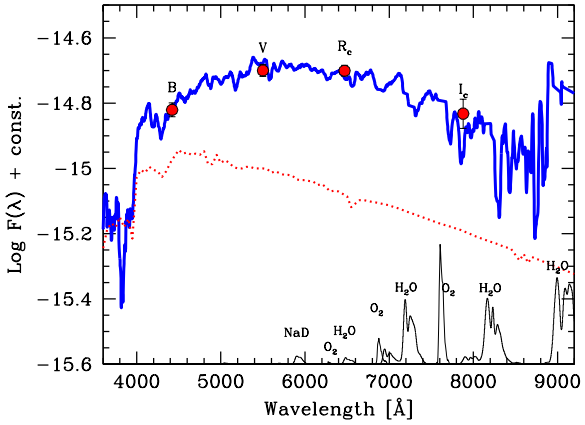

Figure 18: The WT1190F spectrum, taken from Loiano with the BFOSC camera, along the night of 2015 November 12-13. Two 300 s exposures with the grisms GR3 (blue) and GR5 (red) have been matched, spanning the wavelength region 3500-6000 Å with a 2.7 Å px^{-1} dispersion, and 5300-9500 Å with a 4.0 Å px^{-1} dispersion, respectively. The spectral resolving power was degraded here to roughly 100 Å FWHM to improve the S/N ratio still maintaining the relevant shape of the SED. Correction for O_2 and H_2O telluric absorption (according to the pattern sketched in the figure, in arbitrary units, as labelled) has been carried out as discussed in the text. A consistent comparison with B, V, R_c, I_c multicolor photometry (as from Table 3 data) is displayed (big red dots), by converting the mean magnitudes into monochromatic fluxes, according to Buzzoni (2005). The solar spectrum is displayed (red dotted line) with arbitrary offset, for comparison.

colors of Table 3 as a reference, this figure can be converted to the B, V, and I_c band correction as

$$\left.\begin{array}{lllll} Bol - V &= (Bol - R_c) &-(V - R_c) &= -0.41_{\pm 0.05} \\ Bol - B &= (Bol - V) &-(B - V) &= -1.33_{\pm 0.06} \\ Bol - I_c &= (Bol - R_c) &+(R_c - I_c) &= +0.46_{\pm 0.05}. \end{array}\right\} \quad (11)$$

A supplementary and noteworthy piece of information comes, however, when assessing WT1190F in its blue versus near-infrared luminosity, as in the $(R_c - I_c)$ versus $(B - R_c)$ color plot of Fig. 17. A clear departure from the stellar locus appears in this case, with an exceedingly "blue" $(R_c - I_c)$ color, suggestive of a reduced reflectance in the I_c band.

In order to get further hints on the WT1190F composition, in the figure we also compared the observed colors with a number of lab estimates for different materials extensively used in spacecraft and rocket assembly, as collected by Cowardin (2010a) and Cowardin et al. (2010b). Interestingly enough, it appears that the WT1190F texture tends to recall somewhat "grey" materials, like Mylar or Aluminized Kapton layers. This feature is further reinforced by the close resemblance with Planck, in Fig. 15, a "bright silver" spacecraft,[12] with an extended reflective surface that had to mirror the solar spectral distribution.

5.2. *Reflectance properties*

The observed shining properties of WT1190F are the direct result of its reflective response to the solar illumination. This output tightly depends on the size and geometrical structure of the body as well as on its physical composition and surface texture. From a purely empirical point of view, the target reflectance could be assessed, in principle, as a ratio between received and scattered solar flux at a given wavelength interval, providing to know or assume *a priori* the absolute size of the object and the exact scattering law of its surface. In lack of these relevant quantities, one can only aims at a *relative* reflectance estimate, within a constant scale factor.

In this framework, the "depressed" I_c emission of Fig. 17, implicit in the $(R_c - I_c)$ color, is possibly a decisive signature to settle the real nature of WT1190F. This feature is actually confirmed in much finer detail also by the November 13 spectrum, shown in Fig. 18. The plotted SED was obtained by connecting the GR3 (blue) and GR5 (red) spectra in order to sample the full wavelength range from 3600 to 9500 Å, at a nominal step of 3 Å. Special care has been devoted, in the spectral reduction, to consistently account for the strong telluric absorption of molecular oxygen (O_2) and water vapour (H_2O), both affecting the $\lambda \geq 6800$ Å wavelength region due to the wet weather conditions along the observing night.

[12] For extensive information on the Planck mission, see the URL: *http://www.esa.int/Our_Activities/Space_Science/Planck_overview*.

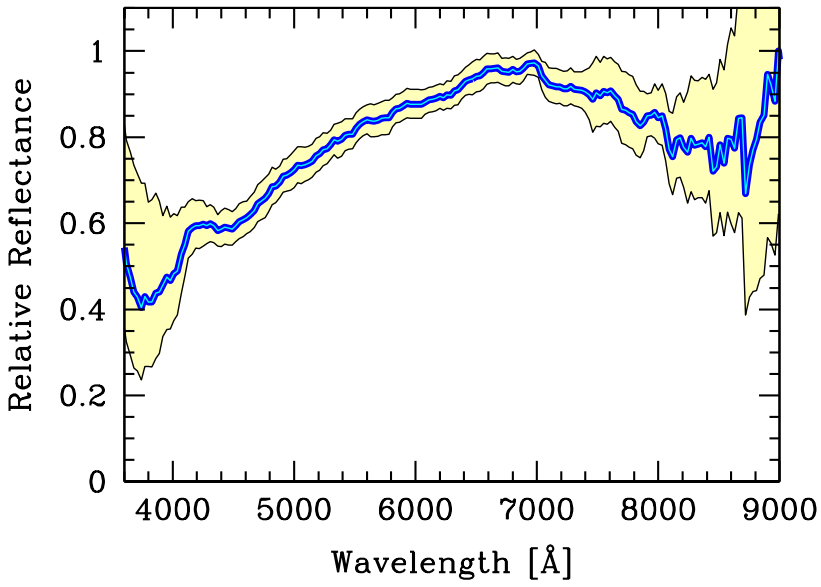

Figure 19: The WT1190F relative reflectance computed by dividing the observed flux of Fig. 18 by the synthetic solar spectrum. The resulting ratio was finally normalized to a unity peak. For its sharply reduced response about 4000 Å and a shallower dip, about 8500 Å, the curve may be suggestive of a prevailing presence of Aluminum in the surface texture of the object.

A standard correction scheme was devised, to this task, by rescaling first a template absorption spectrum of both the O_2 and H_2O band systems, and subtracting then in a parametric way the synthetic pattern from the observations until an acceptable solution was reached. The template spectrum for H_2O was obtained from the theoretical package SPECTRA[13] (Mikhailenko et al., 2005), while the O_2 band system was best modelled empirically, by relying on our own past observations.

In any case, the most conservative approach to the data was pursued, rejecting the poor S/N observations for $\lambda > 9200$ Å, and retaining in addition only those wavelength regions where the observed flux were affected by less than 10% by the intervening O_2 or H_2O absorption. The corrected spectrum was finally smoothed to roughly a 100 Å wavelength resolution to improve the S/N ratio still maintaining the relevant shape of the SED. A consistency test with multicolor photometry was accomplished, at this point, by comparing with the flux-converted BVR_cI_c magnitudes (according to Buzzoni's, 2005, calibration), as reported in Fig. 18.

Although hampered by a slightly poorer S/N toward NIR wavelength, the figure clearly shows a broad and statistically significant bump about 8500 Å, while at the blue-end tail of the spectrum a peculiarly enhanced "4000 Å break" (compared to a nominal K-type "proxy star", as from Fig. 15) may also be noticed.

Relying on the observed SED, the WT1190F relative reflectance ($\Re$) was computed as $\Re_\lambda = k(f_{\rm WT}/f_\odot)_\lambda$, that is by dividing the observed flux ($f_{\rm WT}$) by the synthetic solar spectrum ($f_\odot$), the latter as provided by the Vilnius spectral library of Straizys & Sviderskiene (1972). The resulting ratio was finally normalized to a unity peak, as displayed in Fig. 19. The curve neatly confirms our previous remarks, that is a sharply ($\sim -50\%$) reduced response about 4000 Å and a shallower ($\sim -20\%$) dip, about 8500 Å. This pattern could be suggestive of a prevailing presence of Aluminum in the surface texture of WT1190F (e.g. Henninger, 1984).

6. Toward disclosing WT1190F's possible identities

The emerging picture from the observations definitely points to an artificial nature of WT1190F. A nearly flat absolute magnitude dependence on the phase angle, together with a high inferred AMR figure (Gray, 2015), a flaring lightcurve and a "grey" surface texture, are all clues consistent with a man-made artifact, most probably a relic of a past lunar mission.

In addition, a still remarkable residual spin of the body indicates that, since its release, the interaction with the terrestrial magnetic field has been only a marginal one, preventing the eddy currents to efficiently dissipate the target momentum (e.g. Williams & Meadows, 1978). From one hand, this may call for a relatively young age (a couple of decades, or so) for WT1190F. The chaotic orbital motion may even support this scenario, as a longer in-orbit lifetime would have greatly increased the probability of a Moon impact (e.g. Rickman et al., 2014). On the other hand, the same weak gravitational boundaries with the Earth-Moon system could suggest otherwise an opposite

[13] http://spectra.iao.ru/

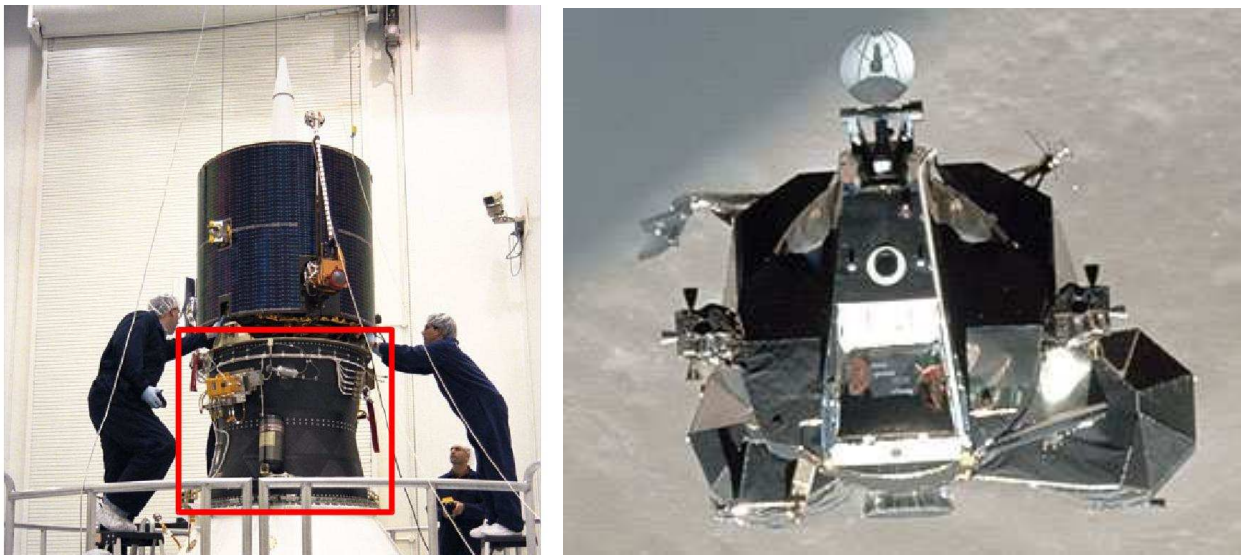

Figure 20: Left panel: the Lunar Prospector spacecraft with its Trans-Lunar Injection Stage (TLIS) framed within the red box. Picture is courtesy of NASA and it is publicly available at the URL: *http://images.ksc.nasa.gov/photos/1997/high/KSC-97PC-1806.jpg*. Right panel: the Lunar Module LM-4 "Snoopy" of the Apollo 10 mission. The picture was taken on May 23, 1969, with "Snoopy" in its course from the Moon to dock again with the Command Module "Charlie Brown". Picture is courtesy of NASA and it is publicly available at the URL: *http://spaceflight.nasa.gov/gallery/images/apollo/apollo10/html/as10-34-5112.html*.

evidence, by setting the case in a more historical context. It could be, in fact, that in its 2009 discovery WT1190F was in a returning path to Earth, after being recaptured from a heliocentric orbit.

If the latter is the case, then the object could be much older and its origin should be moved back to the pioneering lunar missions of the 60's. At least two further examples can be reported on this line, dealing with the puzzling "NEO" objects J002E3 (Jorgensen et al., 2003) and 2010 KQ (Miles, 2011), respectively identified as the Saturn V upper stage of the Apollo 12 mission, in year 1969, and a Blok-L upper stage of a Molniya rocket to be associated with one of the launches of the Russian Lunik missions in the early 60's.

According to the two "young" and "old" scenarios, mentioned before, the current debate on WT1190F's ultimate identity (Birtwhistle, 2015; Gray, 2015; McDowell, 2015a,b; Stockton, 2015; Jenniskens et al., 2016; Watson, 2016) basically focus on two prevailing candidates. In particular, the Athena II Trans-Lunar Injection Stage (TLIS), that carried the Lunar Prospector probe to the Moon in year 1998 (left panel in Fig. 20), seems to be the most viable "young" candidate. On the other hand, a 47 year old contender could be identified in the ascent stage of the lunar module (LEM LM-4) "Snoopy" (right panel in the same figure), released in heliocentric orbit on 1969 May 23, after completion of the Apollo 10 mission.

6.1. Size estimate

To help disentangle between the two candidates, any direct and independent assessment of WT1190F absolute size could evidently provide a crucial step forward. Based on the inferred R_c absolute magnitude of eq. (4) and the expected bolometric correction of eq. (10) we eventually obtain for the object a bolometric magnitude

$$Bol^{\rm abs} = 32.45_{\pm 0.31} + 0.13_{\pm 0.05} = 32.6_{\pm 0.3}. \qquad (12)$$

Following Buzzoni et al. (2016), this figure closely relates to the effective size (s') of an object of physical scalelength (s) and Bond albedo (α), under Lambertian reflectance conditions, so that $s' = s\sqrt{\alpha}$. Inserting eq. (12) into eq. (2) of Buzzoni et al. (2016) we therefore get

$$s = \frac{s'}{\sqrt{\alpha}} = \frac{216_{\pm 30}}{\sqrt{\alpha_{10}}}\ {\rm cm} \qquad (13)$$

with $\alpha_{10} = \alpha/0.1$. As summarized in Fig. 21, the equation indicates that the same target brightness could be provided either by a big and dark object (say a "rugged" 3-meter sized spacecraft with $\alpha \ll 0.1$) or a smaller and lighter one (say a "polished" 1-meter sized module with $\alpha \sim 0.3$).

A word of caution is in order, however, for a more general application of these results as a pure Lambertian scatter surface may poorly apply to man-made space devices, often consisting of polished and mirroring surfaces, unless degraded by extended interaction with space environment.

6.2. The problem of the Area-to-Mass Ratio

As already briefly mentioned in Sec. 4.2, for a proper fit of the astrometric observations of WT1190F it is essential to consider the effects of SRP. The importance of introducing at least a rough modeling of SRP is twofold: from one hand, it is essential to properly model the object motion on long temporal arcs, because the drift from a gravity-only solution becomes evident in the astrometric residuals and consequently affect the trajectory determination; on the other hand, since the SRP acceleration is

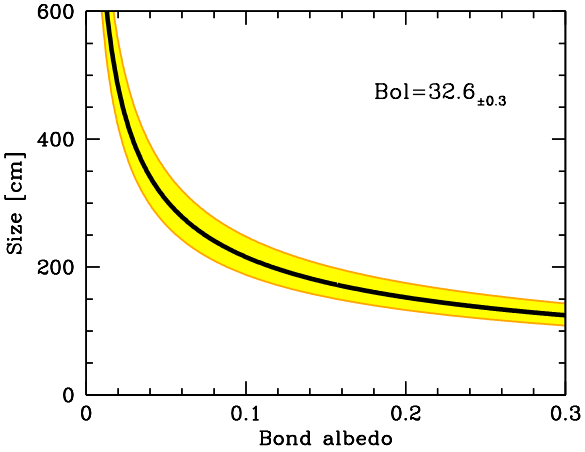

Figure 21: The expected size versus Bond albedo relationship for WT1190F, according to eq. (13). A bolometric absolute magnitude $Bol = 32.6 \pm 0.3$ is assumed for our calculations together with a Lambertian scattering law for the reflecting body.

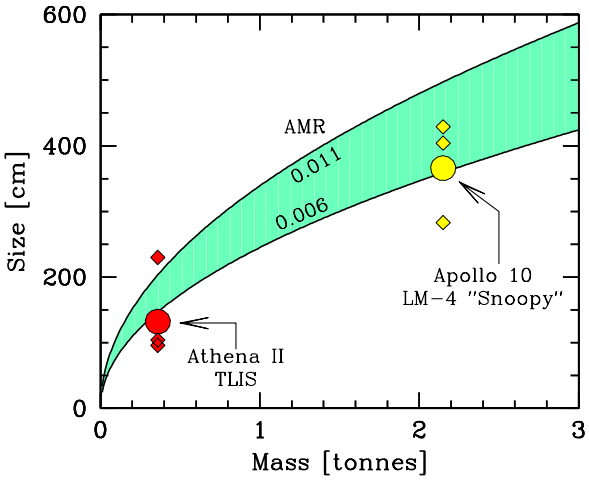

Figure 22: The expected location of the Apollo 10 LM "Snoopy" and the Lunar Prospector TSLI upper stage in the mass versus size domain, compared with the theoretical locus for the AMR ranging between 0.011 and 0.006 $m^2\ kg^{-1}$, as labeled on the plot. For each object, an "effective size" is derived (big dots) as the geometric mean of the corresponding three dimensions (small diamonds in the plot). This is $(2.83 \times 4.04 \times 4.29)^{1/3} = 3.66$ m for Snoopy and $(1.00 \times 1.00 \times 2.30)^{1/3} = 1.32$ m for TLIS. Notice that, in spite of the large structural difference, both "Snoopy" and the TSLI module consistently match the AMR lower envelope, that is for AMR $\sim 0.006\ m^2\ kg^{-1}$.

directly dependent on the AMR of the object, it allows us to indirectly estimate a key physical property of the body, in order to validate its possible identification.

In the case of WT1190F, using the longer dataset of observations available in the literature for the entire 2015 apparition, it is possible to derive a best-fit estimate

$$\mathrm{AMR} = 0.0115\,\mathrm{m}^2\ \mathrm{kg}^{-1}, \tag{14}$$

with a formal error of about 1%. Although in agreement with previous estimates (Gray, 2015), our calculations show that a simple SRP model *does not seem to properly fit all the 2015 data*, other forces likely being in play. Using different subsamples of the same dataset therefore leads to estimates that differ much more than the formal error, actually allowing figures as low as 0.0063 $m^2\ kg^{-1}$ (within a 3% uncertainty), as found in alternative orbit solutions.[14] This behavior is commonly seen in artificial objects, and it is likely due to the combination of two distinct factors:

1. the object has a variable orientation and exposes an ever-changing cross section to the Sun, thus resulting in a truly variable exposed area, and consequently a change in the AMR.

2. the motion of the object is subtly affected by other physical phenomena, mainly the Yarkovsky effect (Bottke et al., 2006), which are capable of imparting an additional acceleration to the object along a direction that depends on its rotational state and thermal properties. In an SRP-only model the other fit parameters, including the AMR, will attempt to "compensate" for any offset, and consequently "torque" the estimate away from its physical value. More specifically, the Yarkovsky effect, well-known for its ability of imparting a tangential torque to the motion of an asteroid, also has a radial component generated by all the heat that happens to be re-emitted in an approximately solar direction. This thermal energy creates a recoil on the object that acts in a way that is practically indistinguishable from the true reflection-based SRP, and is only "delayed" by a time comparable with the thermal inertia scale of the object. It is reasonable to assume that for a metal object such a contribution may be large, and may significantly contribute to the non-gravitational acceleration of the object in the solar direction.

Unfortunately, modeling such forces is not feasible in this case, since it would require the full knowledge of the instantaneous rotational state of the body at any given time. It is nevertheless important to note that they can significantly affect the interpretation of any AMR value derived from dynamics as a true measurement of the physical properties of the body.

The expected AMR figures for both the Snoopy ascent stage and the TLIS rocket upper stage are contrasted in Fig. 22 with the inferred range for the WT1190F. While the (dry) mass of each candidate is reasonably well known, the ever changing cross-sectional area, due to the spinning motion, is prone to a much higher uncertainty leading the resulting AMR value to change. In the figure, the geometric mean of the three dimensions was adopted as the "effective size" for each candidate. The individual size of each dimension, as marked in the plot give a measure of the possible range in the resulting AMR figure. Notably enough, in spite of the quite different mass and size, both Snoopy and TLIS display in fact a very similar ratio about

[14] See, for instance, Gray's alternative calculations at the URL: *http://www.projectpluto.com/tles/wt1190f.tle*.

AMR ~ 0.006 m^2 kg^{-1}, that is consistent with the lower envelope of the WT1190F inferred range. This leads to an implied density of the order of 45 and 160 kg m^{-3}, respectively, for the two hollow objects.

6.3. Mockup rendering and synthetic photometry

An independent assessment of WT1190F's ultimate nature could greatly benefit from a direct comparison of observations with the expected photometric signature as from a careful modeling of the two *bona fide* candidates. This is evidently not quite a straighforward task, as the complex mockup geometry for both Snoopy and the TLIS module has to be properly taken into account, also considering the specific texture of the composing materials in order to lead to a realistic estimate of the inherent object brightness under Sun's illumination.

Mockup modeling was carried out by means of the 3D CAD design software SolidWorks, while mesh rendering relied on the open-source suite MeshLab. An inverse ray-tracing technique was adopted to assess the model photometric properties. In particular, the objects are modeled using rendering via triangular flat surfaces. One ray per facet is casted to illuminate the surface. The self-shadowing is computed via triangle intersection (Moeller, 1997; Shirley, 2002), in barycentric coordinate formulation. Obstruction in both directions, illumination from the Sun and obstruction of the reflected light towards the observer have been taken into account. Larger flat surfaces are subdivided, in order to allow for precise modeling especially for the self-shadowing effects (see, e.g. Frueh & Jah, 2014).

If a facet is under Sun's illumination through an angle β from its normal direction[15], then the received flux at the observer's location, placed at a reference distance d (Hapke, 1993), is

$$f_{out} = \epsilon_{\rm ss} \, [\frac{f_\odot \, \omega^2}{4\pi} \, \psi(\gamma) \, \cos(\beta)]. \tag{15}$$

In the equation, $f_\odot$ is the incident bolometric flux from the Sun, ω^2 is the apparent angular surface of the emitting facet (in steradians), as seen from the observer, and $\psi(\gamma)$ is the bidirectional reflection function (BRDF), that accounts for facet orientation and texture properties. [16]

A self-shadowing cut-off factor ($\epsilon_{\rm ss}$, normally set at 1) may eventually be introduced in the equation, to "switch off" the output ($\epsilon_{\rm ss} = 0$) if the relevant facet happens to be either in shadow or invisible to the observer, according to target geometry.

For the BRDF computation, a combination of Lambertian, specular reflection and absorption has been adopted. More complex reflection models do exist, however in the absence of exact surface data this simple model was chosen as a robust baseline estimate. In eq. (15), the function $\psi(\gamma)$ modulates the facet emission toward the observer. The relative partition between diffuse and specular reflection is accounted for by the corresponding (bolometric) C_d and C_s coefficients, both depending on the facet texture properties. In its more general form (e.g. Hapke, 1993), $\psi(\gamma)$ can therefore be written as

$$\psi(\gamma) = \frac{C_d}{\pi} \, \cos(\gamma) + \epsilon_{\rm mirr} \, \frac{4\pi}{\Omega_\odot^2} \, C_s, \tag{16}$$

where $\Omega_\odot^2$ is the Sun's apparent angular surface (in steradians), as seen from the facet, and γ is the observer's direction, seen through an angle γ with respect to the facet normal.[17] By default, in the equation, the facet is assumed to scatter the incident solar flux (so that the cut-off factor $\epsilon_{\rm mirr}$ is normally set to zero) unless the mirroring condition is fulfilled– namely $(\beta - \gamma) = 0 \pm 0.25^o$, where a half degree full tilt is still allowed to account for Sun's finite angular diameter– and $\epsilon_{\rm mirr}$ is then turned to 1.

Once eq. (15) is computed for each facet of the object mockup, then the total exitant bolometric luminosity simply derives as a sum over the model: $f_{tot} = \sum f_{out}$, and the figure can then be converted into an absolute bolometric magnitude (M_{bol}) if we take $d = 1$ au, or $1.49\,10^{13}$ cm and set the photometric zero point by scaling with the solar figures, namely

$$M_{bol} = m_\odot - 2.5 \log f_{tot} + 2.5 \log f_\odot. \tag{17}$$

By assuming for the Sun an apparent bolometric magnitude and incident flux at Earth (outside atmosphere) of $m_\odot = -26.85$ and $f_\odot = 1.353\,10^6$ erg cm^{-2} s^{-1}, respectively (e.g. Lang, 1980), then eq. (17) eventually provides

$$M_{bol} = -2.5 \log f_{tot} - 11.52, \tag{18}$$

providing to express f_{tot} in cgs units.

6.3.1. The Lunar Prospector TLIS rocket upper stage versus the ascent stage of the Apollo 10 LEM "Snoopy"

Our own mockup of the TLIS rocket upper stage was created according to the published dimensions (Adolz et al., 1998) and by judging from photographic imagery (as in the left panel of Fig. 20). The final rendering featured 2902 facets. Our result is shown in the left panel of Fig.23. We assumed a main body made of Aluminum liner with a Graphite epoxy overwrap (Adolz et al., 1998). The body appears almost completely black in color, with almost no specular component and a constant Lambertian reflection coefficient such as $(C_d, C_s) = (0.1, 0.0)$. The

[15] Angle β is often referred to as the "solar aspect angle".

[16] Note that the factor 4π remains sometimes implicit in other notations of eq. (15) (e.g. Frueh & Jah, 2014), when dealing for instance with the *exitant intensity* instead of the *received flux* at the observer. See, e.g., Hapke (1993) for a clearer settlement of definitions and reference theoretical framework, in this regard.

[17] The angle γ is often referred to as the "Earth aspect angle". Note that in the illustrative case of a body consisting of just one planar facet, both γ and β relate to the "phase angle" of the previous discussion as $\phi = \beta + \gamma$.

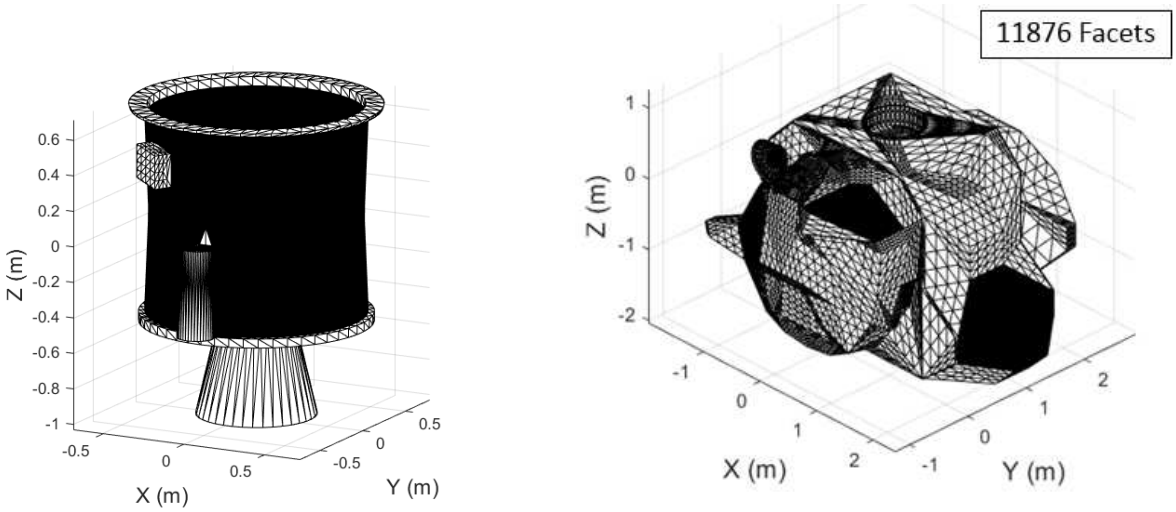

Figure 23: The rendered TLIS (left panel) and Snoopy (right panel) mesh models. A total of 2902 and 11876 facets have been assumed for the two targets, respectively.

bright ring and the nozzle, as well as the other smaller features, were modeled assuming an Aluminum-coated Mylar texture (Funge, 2005), then with a set of BRDF coefficients $(C_d, C_s) = (0.9, 0.1)$.

A publicly available 3D Studio model has been used for the Snoopy ascent stage.[18] The original model has 9588 single surface facets. It includes the detailed mapping of smaller features, like the attitude control nozels, the handrails, which are overall very small, however are very densely sampled. In a first step, the model has been ridded of the smaller features, reducing the number of facets down to 1352. Mesh partition was then increased, up to a total of 11876 facets, using a midpoint sub-division algorithm in MeshLab. This is to lead to a more accurate ray tracing in order to properly account for partial self-shadowing conditions across the LEM surface, depending on Sun's illumination circumstances (see Fan et al., 2016, for further technical details)

Deriving material components, especially with the unknown ageing effects, poses a significant challenge. As those are largely undetermined at the moment, and no reliable data could be secured, educated guessed on the original materials were made. As for the TLIS module, an Aluminum-coated Mylar has been chosen also for Snoopy's highly reflective materials, based upon the spacecraft photographic pictures (as in the right panel of Fig. 20). For them we assumed, again, $(C_d, C_s) = (0.9, 0.1)$. Black surfaces where rendered, on the contrary, by assuming a Silicon carbide (SiC) composition with a constant Lambertian reflection such as $(C_d, C_s) = (0.1, 0.0)$. The SiC choice was motivated by its wide use as antioxidant paint in space applications. The final mockup of the LEM ascent stage is shown in the right panel of Fig. 23.

[18] See the URL: *http://www.sharecg.com/v/67738/view/5/3D-Model/Apollo-Lunar-module-and-ALSEP*, for model download.

6.3.2. Synthetic lightcurves versus phase angle

A realistic analysis of the derived photometric features of both the TLIS and Snoopy models should forcedly restrain to two main parameters, namely the expected absolute magnitue $Bol_o^{\rm abs}$ at vanishing phase angle and the rate at which magnitude fades with increasing ϕ, namely $dBol/d\phi$ mag deg^{-1}. Both figures can consistently be compared with the data of Fig. 5, once accounting for eq. (12) to convert R_c photometry to bolometric.

No further attempt has been carried out, in this regard, to match the observed quick-spinning lightcurves of Fig. 11 and 12, as the fully unknown attitude properties of WT1190F would make completely aleatory our conclusions. Quite importantly, however, one can be assured that, for a given illumination conditions, the very short spinning/tumbling period of WT1190F allows the synthetic magnitude of each *bona fide* candidate to consistently comes from an average across the full range of the Euler angles to sample objects' attitude.

Once accounting for Lambertian-only BRDF in eq. (16) (that is by preliminarily setting $\epsilon_{mirr} = 0$, throughout), our synthetic photometry for Snoopy and TLIS compares with the WT1190F fitting relation as in Fig. 24. At $\phi = 0$, our Snoopy ascent stage model displays an absolute bolometric magnitude $Bol_o^{\rm snoopy} = 31.36_{\pm 0.15}$, while the TLIS rocket upper stage model appears fainter, with $Bol_o^{\rm TLIS} = 33.35_{\pm 0.06}$. The scatter, for both models has been estimated from the synthetic photometry, by randomly changing mockup's orientation. In addition to the $\phi = 0^o$ case, the same trial was then further repeated at seven different phase angle values in the range $0^o \leq \phi \leq 105^o$. As evident from the figure, a drastic increase of model rms (that is a larger "flickering" of object's magnitude) when the Sun begins to illuminate "from behind" ($\phi \geq 90^o$). By "switching on" specular reflection in eq. (16) we would obtain models that are in general about 0.5 mag brighter, although with

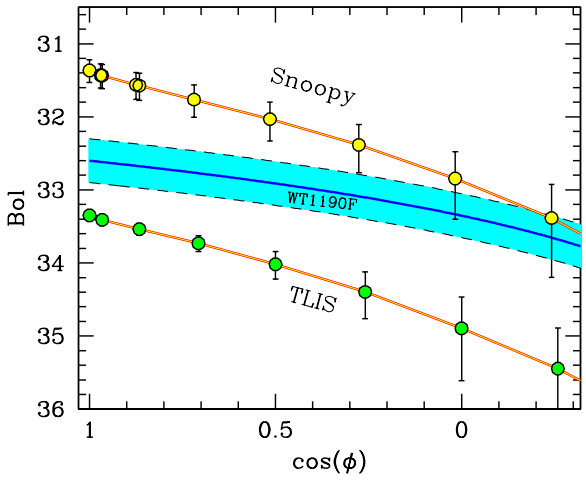

Figure 24: The absolute magnitude of Snoopy and TLIS mockups, with varying the phase angle ϕ, according to our synthetic photometry, is compared with WT1190F's observations. The latter are from Fig. 5, once accounting for eq. (12) to convert R_c photometry to bolometric. If Lambertian reflection is assumed in our BRDF treatment, at $\phi = 0$, the Snoopy mockup displays an absolute magnitude of $Bol_o = 31.36_{\pm 0.15}$, while a corresponding value of $33.35_{\pm 0.06}$ is obtained for the TLIS rocket upper stage. Notice for both models a steeper trend than WT1190F's absolute luminosity with increasing the orbital phase angle, ϕ. Error bars are attached to average magnitudes for each ϕ configuration as the rms of some 150 individual estimates, by randomly changing mockup's orientation in our synthetic photometry.

a much increased scatter among individual measurements. However, the latter might barely be the real case, we believe; from one hand, a nearly half-a-century interaction with deep-space environment could have heavily degraded Snoopy's polished body texture. On the other hand, the TLIS module spots by itself an intrinsically opaque and dark texture, with only a negligible fraction of reflective facets.

In spite of a very different shape, both Snoopy and TLIS are found to behave very similarly from a photometric point of view, with their absolute magnitude becoming fainter with increasing ϕ at a rate of $dBol/d\phi \sim 0.017_{\pm 2}$ mag deg^{-1}. As expected, according to its absolute magnitude, TLIS appears to be a factor of 2.5 smaller in effective size (s') compared to Snoopy, a figure that consistently compares with the physical scalelength ratio of both objects, as from Fig. 22, namely 3.66/1.32 = 2.77. As we outlined in Sec. 3.1, the magnitude trend with ϕ is steeper than what we observed for WT1190F but flatter than a typical asteroid figure and even flatter than a theoretical Lambertian sphere (e.g. Hapke, 1993, as we directly verified through our computations).

In principle, a "rugged" Snoopy with a factor of three lower albedo, or a factor of two brighter albedo for TLIS might lead either models to match WT1190F's absolute magnitude, but a substantial deviation from the Lambertian reflection regime (namely in the sense of a "broader" BRDF profile, like for instance in a Phong, 1973 model) should be invoked in both cases, in order to account for WT1190F's photometric behaviour at large phase angle.

7. Summary and conclusions

The puzzling case of WT1190F, discovered by the Catalina Sky Survey group in October 2015, raised awareness about the intriguing nature of this object, likely a man-made relic of some past lunar mission, of unknown origin and at some time left in chaotic orbit beyond the Moon. Its final fate, with Earth collision on 2015 November 13, offered a suggestive connection with the envisaged scenario in the event of a natural (and far more dangerous) impactor, like an asteroid or a comet, and this added a special point of interest for its observation, as a realistic simulation and training for what kind of data would be possible to obtain in this extreme circumstance. As part of the worldwide observing campaign (see, e.g., Micheli et al., 2018, for a brief discussion), we have been reporting in this paper on the combined observations of WT1190F from Italy and Spain (respectively the Loiano and DeSS Observatories) to further constrain the physical and dynamical characteristic of this special object.

The remarkably small variation of WT1190F R_c absolute magnitude with changing orbital phase angle (ϕ), i.e. $dR_c/d\phi \sim 0.007_{\pm 2}$ mag deg^{-1} (Fig. 5) led us to estimate $R_c^{\rm abs} = 32.45_{\pm 0.31}$ mag (at $\phi \to 0^o$ and scaled at 1 au) lending support to an artificial nature of the object (Frueh & Schildknecht, 2010; Cowardin et al., 2012; Murtazov, 2013).

In its final approach to Earth, down to a minimum range distance of 12,500 km, until about 34 minutes before the final impact with the Indian Ocean, WT1190F was extensively tracked in the V band with the DeSS telescopes, accompanied by BVR_cI_c multicolor photometry from Loiano (Fig. 8). The decreasing distance, also eased a long-slit spectroscopy to probe in fine detail the object reflectance characteristics along the 3500-9000 Å wavelength range. The observed SED (see Fig. 18) revealed a moderately blue-depressed body, consistent with a star of spectral type K3 (Fig. 15). In addition, the derived reflectance curve of Fig. 19 also showed a broad "dip" in the $\sim$ 8500 Å spectral region leading to a I_c-depressed flux. Overall, WT1190F's reflectivity properties seem consistent with a somewhat "grey" surface texture, like that displayed by Mylar or Aluminized Kapton layers (Cowardin, 2010a; Cowardin et al., 2010b).

Superposed to the wild photometric behaviour of WT1190F along the last approaching phase (see Fig. 9), a regular lightcurve was eventually detected in the last minutes (Fig. 11), with a leading period $P_{\rm flash} = 1.4547_{\pm 0.0005}$ s and amplitude of about 1.1 mag. The abrupt setting of a secondary maximum (Fig. 12), at orbital phase angle $\phi > 90^o$ led us to conclude that WT1190F consisted in fact of four mirroring facets (roughly at orthogonal directions) so that the physical spinning period for the

body may have been twice the nominal duty cycle, namely $P_{\rm spin} = 2.9094_{\pm 0.0003}$ s.

The spinning pattern can even be recognized along the WT1190F fiery entry (see Fig. 13) when, according to Farnocchia's (2015) final orbit reconstruction, the body crossed Earth's atmosphere with a steep incident angle ($\sim 20^o$) and at hypersonic velocity (10.6 km s^{-1}). Following Jenniskens' et al. (2016) thorough analysis, there are reasons to believe that the quick spinning motion may have partly shielded the body from the disruptive thermal shock along the fireball phase. As a consequence, possibly a large fraction of WT1190F could have survived the entry event and reached the Indian Ocean.

By merging the Loiano and DeSS astrometric data, the WT1190F ballistic impact point with the ocean surface off the coast of Sri Lanka can be located at coordinates 5.6299^o N, 81.4898^o E, with a formal uncertainty of only $\pm$400 m (mostly in the motion direction) and 0.1 s on the impact timing. The intervening effect of the atmosphere drag on the fragmented body might, however, have largely anticipated the real impact point of the debris by up to 80 km before the nominal ballistic solution. Of potential interest in case of any future submarine mission aimed at recovering the WT1190F wreck, survived debris might likely lie underwater, at a depth of some 1500 meters or even shallower (Fig. 14). Perhaps two thirds of the WT1190F mass may be hidden there (Jenniskens et al., 2016).

According to WT1190F's inferred bolometric luminosity, $Bol^{\rm abs} = 32.6_{\pm 0.3}$, an effective size of the body (s') was implied, under Lambertian surface scatter, such as $s' = s\sqrt{\alpha/0.1} = 216_{\pm 30}$ cm (Buzzoni et al., 2016) (Fig. 21). Both a 3-meter sized spacecraft with a coarse surface texture (as for $\alpha \ll 0.1$), like the Apollo 10 LEM ascent stage, callsign "Snoopy", and a polished 1-meter sized body with $\alpha \sim 0.3$, like the Lunar Prospector TLIS rocket upper stage, could in principle be compatible with the observations. With a similar figure of AMR ~ 0.006 m^2 kg^{-1}, both candidates also match the allowed range for the WT1190F AMR ratio, as inferred from the SRP perturbation on the body trajectory (see Fig. 22).

Accurate mock-up modelling and BRDF reflectance rendering (Hapke, 1993) for Snoopy and the TLIS module has been carried out in Sec. 6.3, in order to reproduce synthetic photometry to be compared with the observed dataset. The resulting absolute magnitude (at "face-on" illumination conditions) are $Bol^{\rm abs} = 31.36_{\pm 0.15}$ and $Bol^{\rm abs} = 33.35_{\pm 0.06}$, respectively. Again, under realistic physical circumstances, both the LEM ascent stage and the TLIS upper stage may in principle be consistent with WT1190F. However, while a somewhat "ad hoc" brightening in the TLIS albedo should be required to match the observed WT1190F magnitude, a more plausible "darkening" in Snoopy's albedo may be conceived as a consequence of strong ageing effects, after so long a journey around the Sun. Alternatively, a hint exists for a possible "outsider" candidate to WT1190F's identity to be about 50% bigger than the Athena II TLIS upper stage. In any case, none of the two mockups can reproduce the flat trend observed for WT1190F absolute magnitude versus orbital phase angle ϕ (see Fig. 24), perhaps a sign of a substantial deviation of the WT1190F BRDF properties from the Lambertian regime, like in some $cos^n(\gamma)$ generalized Phong (1973) reflectance models.

References

Altavilla G., Foppiani I., Micheli M., Bruni I., Gualandi R., Buzzoni A. 2015, DASO Circ. No. 539, IAU Minor Planet Center, ed. G. V. Williams

Andolz F. J., Dougherty T. A., Binder A. B., 1998, Lunar Prospector Mission Handbook, Lockheed Martin Missile and Space Company, Document No: LMMS/P458481.

Birtwhistle P., 2015, the Great Shefford Obs. web site at *http://peter-j95.blogspot.it/2015/11/the-life-and-death-of-wt1190f-uda34a3.html*

Borovička J., Charvát Z., 2009, A&A, 507, 1015

Borovička J., Abe S., Shrbený L., Spurný P., Bland P. A., 2011, PASJ, 63, 1003

Borovička, J., Spurný, P., Brown, P., Wiegert, P., Kalenda, P., Clark, D., Shrbený, L., 2013, The trajectory, structure and origin of the Chelyabinsk asteroidal impactor, Nature 503, 235-237.

Bottke W. F., Jr., Vokrouhlický D., Rubincam D. P., Nesvorný D., 2006, AREPS, 34, 157

Buratti B. J., Hillier J. K., Wang M., 1996, Icar, 124, 490

Buzzi L., Colombo G., 2015, the "G. Schiaparelli" Observatory at Campo dei Fiori web site at *http://www.-astrogeo.va.it/astronomia/detritoWT1190F.php*

Buzzoni A., 2005, MNRAS, 361, 725

Buzzoni A., Altavilla G., Galleti S., 2016, AdSpR, 57, 1515

Buzzoni A., Altavilla G., Micheli M., Bruni I., Gualandi, R. 2015b, DASO Circ. No. 532, IAU Minor Planet Center, ed. G. V. Williams

Cowardin H. M., 2010, PhD thesis, Univ. of Houston TX USA

Cowardin H., Seitzer P., Abercromby K., Barker E., Schildknecht T., 2010, amos.conf, E47

Cowardin, H., Lederer, S., Liou, J.-C., Ojakangas, G., Mulrooney, M., 2012, Advanced Maui Optical and Space Surveillance Technologies Conference 61.

Desai P. N., Qualls G. D., 2010, JSpRo, 47, 736

Fan, S., Frueh, C., Buzzoni A., 2016, proc. of the AIAA/AAS Astrodynamics Specialist Conference, AIAA SPACE Forum, (AIAA 2016-5504).

Farnocchia D., 2015, s46 JPL orbit solution, according to the JPL Horizons Solar System Dynamics (SSD) Interface (see URL *http://ssd.jpl.nasa.gov/horizons.cgi*)

Farnocchia D., Chesley S. R., Brown P. G., Chodas P. W., 2016, Icar, 274, 327

Frueh C., Jah M. K., 2014, AcAau, 95, 227

Frueh, C., Schildknecht, T., 2010, in: proc. of the 61st International Astronautical Congress 2010 (IAC 2010), Ed. International Astronautical Federation (IAF), (Red Hook, USA: Curran Associates, Inc.), 194

Fujita K., et al., 2011, PASJ, 63, 961

Funge A. D., 2005, MSc Thesis, Air Force Inst. of Technology, Wright-Patterson Air Force Base, Ohio, USA

Gray W.J., 2015, Project Pluto web site at *http://projectpluto.com/temp/wt1190f.htm*

Hapke B., 1993, Theory of reflectance and emittance spectroscopy, Cambridge University Press: New York, p. 190

Hapke B., van Horn H., 1963, JGR, 68, 4545

Henninger J. H., 1984, NASA Reference Publ. no. 1121 (NASA: Greenbelt, USA)

Jenniskens P., et al., 2004, EM&P, 95, 339

Jenniskens P., et al., 2009, Natur, 458, 485

Jenniskens P., 2010, JSpRo, 47, 718

Jenniskens P., Kozubal M. K., Dantowitz R.F., Breitmeyer J., Winter M. W., Grinstead J. H., Loehle S., 2010. Time-resolved absolute irradiance of the Hayabusa Sample Return Capsule Reentry. 50th AIAA Aerospace Sciences Meeting Including the New Horizons Forum and Aerospace Exposition, (AIAA 2012-1294), 31
Jenniskens P, et al., 2016, Proc. of the AIAA Sci. and Tech. Forum and Exposition (SciTech 2016), San Diego, CA
Jorgensen K., Rivkin A., Binzel R., Whitely R., Hergenrother C., Chodas P., Chesley S., Vilas F., 2003, DPS, 35, 36.02
Lang K. R., 1980, Astrophysical formulae, 2nd edition, Springer: Berlin, p. 562
Landolt A. U., 1992, AJ, 104, 340
Li J.-Y., Helfenstein P., Buratti B., Takir D., Clark B. E., 2015, Asteroids IV, 129
Loehle S., Jenniskens P., 2014. High-resolution spectroscopy of the Hayabusa Reentry using a Fabry-Perot Interferometer. J. Spacecraft and Rockets 51, 1986-1993.
Matheny R.G., et al. 2015, DASO Circ. No. 520, IAU Minor Planet Center, ed. G. V. Williams
McDowell J., 2015, private communication
McDowell J., 2015, Twitter on-line account at *https://twitter.com/planet4589/status/665017832489390080*
Micheli M., Buzzoni A., Koschny D., Drolshagen G., Perozzi E., Hainaut O., Lemmens S., Altavilla G., Foppiani I., Nomen J., Sanchez-Ortiz N., Marinello W., Pizzetti G., Soffiantini A., Fan S., Frueh C., 2018, Icar, in press
Mikhailenko S.N., Babikov Yu.L., Golovko V.F., Atmospheric and Oceanic Optics. 2005. V. 18, No.09. P. 685-695
Miles R., 2011, JBAA, 121, 350
Möller T., Trumbore B., 1997, Journal of Graphics Tools, 2, 21
Murtazov A. K., 2013, Am. J. Mod. Phys., 2, 282
Nelson R. M., Hapke B. W., Smythe W. D., Horn L. J., 1998, Icar, 131, 223
Oke J.B., 1990, AJ, 99, 1621
Pecaut M. J., Mamajek E. E., 2013, ApJS, 208, 9
Phong B. T., 1973, Ph.D. dissertation, Univ. of Utah, Salt Lake City, USA
Popova, O. P., and 59 colleagues, 2013, Chelyabinsk Airburst, Damage Assessment, Meteorite Recovery, and Characterization, Science 342, 1069-1073.
Proud S. R., 2013, GeoRL, 40, 3351
Rickman H., Wiśniowski T., Wajer P., Gabryszewski R., Valsecchi G. B., 2014, A&A, 569, A47
Roeser S., Demleitner M., Schilbach E., 2010, AJ, 139, 2440
Sánchez-Ortiz N., Nomen J. , Hurtado M. 2015, DASO Circ. No. 539, IAU Minor Planet Center, ed. G. V. Williams
Shirley P., 2002, Fundamentals of Computer Graphics, A.K. Peters, Ltd, ISBN 1-56881-124-1.
Stockton N., 2015, Wired (on-line edition) at *http://www.-wired.com/2015/11/last-weeks-downed-ufo-a-rocket-but-no-one-knows-which/*
Straizys V., Sviderskiene Z., 1972, VilOB, 35, 3
Watson T., 2016, Nature, doi:10.1038/nature.2016.19162
Williams V., Meadows A. J., 1978, P&SS, 26, 721
Zacharias N., Finch C. T., Girard T. M., Henden A., Bartlett J. L., Monet D. G., Zacharias M. I., 2013, AJ, 145, 44
Zuluaga J. I., Ferrin I., Geens S., 2013, arXiv, arXiv:1303.1796